Acta Cryst. (1998). A**54**, 971–996

Accurate Charge-Density Studies as an Extension of Bayesian Crystal Structure Determination

Pietro Roversi,[a] John J. Irwin[a] and Gérard Bricogne[a,b]*

[a]*MRC Laboratory of Molecular Biology, Hills Road, Cambridge CB2 2QH, England, and* [b]*LURE, Université Paris-Sud, Bâtiment 209D, 91405 Orsay, France. E-mail: gb10@mrc-lmb.cam.ac.uk*

(*Received 27 January 1998; accepted 8 April 1998*)

Abstract

Many hopes and much controversy have surrounded the application of the maximum-entropy (ME) method to accurate charge-density studies. This paper shows that viewing such studies as an extension of Bayesian crystal structure determination provides practical means of fulfilling many of the hopes invested in the ME method, while essentially eliminating its controversial aspects, the latter being explained in terms of a number of computational artefacts. The positional probability distribution of scatterers having maximum entropy relative to a given 'prior prejudice' is computed so as to reproduce a set of phased structure-factor amplitudes; core electrons can optionally be treated as a fixed 'fragment' and described using atomic core densities derived from *ab initio* wave functions. Fragment and prior-prejudice density distributions are computed by fast Fourier transforms and are thermally smeared by aliasing. These various algorithms have been implemented within the *BUSTER* computer program. Model studies on noise-free synthetic data sets for α-glycine, silicon and beryllium show that all-electron calculations give rise to artefacts when a uniform prior prejudice is used, while valence-only calculations using valence monopole priors are essentially free from artefacts. The maximum-entropy approach is thus optimally implemented by incorporating the prior knowledge of the existence of sharp atomic cores in the form of a fragment not subjected to entropy maximization. These results contribute to settling the debate about the putative existence of non-nuclear density maxima at special positions for crystalline silicon and beryllium, and prepare the ground for developing maximum-likelihood multipolar refinement.

1. Introduction

While attempting to determine crystal structures, crystallographers face various degrees of uncertainty, depending on the amount of structural knowledge already available before the diffraction data are consulted: a variable proportion of information is missing about the unmeasured structure-factor amplitudes and phases. Correspondingly, the actual object referred to as 'crystal structure' spans a large spectrum of different distributions (and map representations), ranging from low-resolution macromolecular envelopes to accurate electron-density maps.

In the past decade, one of us (GB) has outlined a global approach to crystal structure determination that recasts within a single inference scheme the process of recovering missing information and allows various crystallographic problems to be tackled making use of a common computational strategy (Bricogne, 1984, 1988*a*, 1991*b*, 1997). This approach is based on the combined use of structural models and maximum-entropy distributions of scatterers, following the prescriptions of Bayesian statistics.

Partial implementations of this *Bayesian programme* (Bricogne & Gilmore, 1990; Bricogne, 1993*a*) have already proved successful in overcoming the phase problem in a variety of crystallographic contexts, ranging from X-ray single-crystal diffraction for small molecules (Gilmore *et al.*, 1990) and macromolecules (Carter *et al.*, 1990; Xiang *et al.*, 1993; Doublié *et al.*, 1994, 1995; Schiltz *et al.*, 1997) to powder diffraction (Gilmore *et al.*, 1991) and electron diffraction (Dong *et al.*, 1992; Voigt-Martin *et al.*, 1995).

In this paper, we report work on the first stages of extending the Bayesian programme to accurate charge-density studies based on single-crystal X-ray diffraction data. These studies lie at the high-resolution end of the phase uncertainty range, where a wealth of prior phase information is already available from the known spherical-atom structure for the crystal. The residual phase uncertainty to be removed by the structure-determination process amounts in this case to a few degrees at most, and is mainly due to the redistribution of valence electrons in the chemical bonds.

We propose that accurate charge-density studies be viewed as the late stages of the structure-determination process. Although a great deal of phase information is present, the fine structure is missing and can be recovered by means of a statistical analysis of the diffraction data, just as is performed in the early stages of the structure-determination process. The phase uncertainty is again brought down to the level warranted by data resolution and completeness.

ISSN 0108-7673

We will show here that the same inference scheme that is used to solve structures by the joint use of structural models at atomic resolution and maximum-entropy distribution of *atoms* can be extended to the task of deriving a high-resolution charge-density distribution: in this particular case, the process of structure completion will make use of subatomic structural models, namely of the partitioning of the atomic density in core and valence contributions commonly used in multipolar studies, and maximum-entropy distributions of *electrons*.

Within this scheme, it becomes a straightforward matter to obtain maximum-entropy valence-density maps and the corresponding deformation-density maps. The method can be applied to centrosymmetric and noncentrosymmetric crystals. Once the implementation is complete, the joint use of structural models and maximum-entropy distribution of scatterers will also allow flexible modelling of the valence-charge density and simultaneous maximum-likelihood refinement of all those parameters that appear in the model for the substructure not subjected to entropy maximization.

The maximum-entropy method has been used in the field of accurate charge-density studies for some time now (see §2): it does possess the potential of overcoming some of the limitations of traditional multipolar modelling but great care has to be taken not to apply it outside the range of validity of its own foundations. In this paper, we present a rationale for the well known drawbacks of the maximum-entropy method as applied to charge-density studies, which have so far eluded explanation.

After a brief discussion of the main sources of error affecting the present-day implementation of multipolar and maximum-entropy charge-density studies (§2), we apply the Bayesian viewpoint to the same studies (§3). §4 investigates the main sources of bias connected to the use of uniform prior-prejudice distributions. The basic computational mechanism and its current state of implementation within the computer program *BUSTER* (Bricogne, 1993*a*) are outlined in §5. In the final part of the paper, we describe the results of model studies for crystalline silicon and beryllium. A novel algorithm for sampling thermally smeared ('dynamic') model densities on arbitrarily coarse grids, implemented in the course of this work and in connection with the calculation of prior-prejudice distributions, is described in Appendix *A*. Table 1 lists abbreviations used in this paper.

Table 1. *Table of abbreviations*

IAM	Independent-atom model
ME	Maximum entropy
NUP	Non-uniform prior-prejudice distribution
UP	Uniform prior-prejudice distribution
NNM	Non-nuclear density maximum

2. MaxEnt charge-density studies: hopes and fears

2.1. *Model bias in conventional charge-density studies.*

The elimination and/or correction of systematic errors in experimental data is still the primary concern in charge-density studies based on high-resolution X-ray diffraction data; when special care is taken to minimize the errors, these experimental studies can achieve an accuracy better than 1% in the values of the structure-factor amplitudes of the simplest structures (Larsen & Hansen, 1984; Lu *et al.*, 1993). The accuracy for small molecular crystals, although more difficult to assess, is reckoned to be of the same order of magnitude.

The challenge is then to achieve the same degree of accuracy in the derived values of the experimental electron density. Recent studies have shown that in some cases this is indeed within the reach of the present-day modelling techniques (Souhassou *et al.*, 1992; Destro & Merati, 1995; Flensburg *et al.*, 1995; Iversen, Larsen, Figgis & Reynolds, 1997). When the major sources of experimental error have been corrected for, the typical root mean square electron-density residual can reach values as low as $0.05\ \mathrm{e\ \AA^{-3}}$, with extrema below $0.20\ \mathrm{e\ \AA^{-3}}$ in absolute value. The observed residuals are usually due to the errors in the experimental data but high-resolution high-quality data sets can in some cases bring to light bias from the model.

The main sources of model bias in multipolar density studies are: the choice of exponents appearing in the radial parts of the deformation functions, still 'more of an art than a science' (Flensburg *et al.*, 1995); the insufficient radial flexibility in modelling valence-charge density in metals, minerals (Nowack *et al.*, 1991; Brown *et al.*, 1993) and coordination complexes (Iversen, Larsen, Figgis & Reynolds, 1997);† and the limited order of the spherical harmonics used, which do not usually extend past the hexadecapolar level ($l = 4$). The latter limitation is not always imposed by the quality of the data, and can be due to the need to preserve an adequately high observations/parameters ratio. Only two multipolar studies published to date used spherical harmonics with $l > 4$: graphite (Chen *et al.*, 1977) and crystalline beryllium (Stewart, 1977). In the latter work, the most significant contribution to the valence density was indeed shown to be given by a pole of order $l = 6$.

We also recall here that all current implementations of structural refinement, when applied to noncentrosymmetric crystals, violate one of the basic principles in least-squares refinement, namely that all quantities appearing in the equations should be either constants, parameters in the model or observations. Structure-factor phases, which cannot be measured, are treated as

† Similar evidence of the inability of single-exponential deformation functions to account for all the information present in the observations have also been found in studies of organic (Howard *et al.*, 1995; Roversi, Barzaghi, Merati & Destro, 1996) and inorganic (Souhassou *et al.*, 1995) molecular crystals.

constants at each cycle of refinement and assumed equal to the calculated values at the previous cycle, but do undergo changes from one cycle to the next. This problem has recently been brought to general attention in the context of refinement of macromolecular structures, where inappropriate treatment of phases can result in a significant source of variance being absent from the least-squares variance–covariance matrix and in phase bias being locked in by the use of an incomplete model (Bricogne & Irwin, 1996).

In practice, charge-density studies can usually rely on large observations/parameters ratios, which overcome most of the phase bias and allow for accurate results for noncentrosymmetric crystals as well. Nonetheless, it is well known that odd-order multipoles invariant under crystal class symmetry can in some cases give rise to serious difficulties in least-squares refinement of noncentrosymmetric structures (Terpstra *et al.*, 1993; El Haouzi *et al.*, 1996; van Beek *et al.*, 1996). Recourse to maximum-likelihood multipolar refinements would allow the unbiased estimation of all parameters entering the electron-density model.

2.2. *MaxEnt charge-density studies*

Because of the limitation intrinsic to the adoption of an explicit parameterized density model, many crystallographers have been dreaming of disposing of such models altogether. The thermally smeared charge density in the crystal can of course be obtained without an explicit density model, by Fourier summation of the (phased) structure-factor amplitudes, but the resulting map is affected by the experimental noise, and by all 'series-termination' artefacts that are intrinsic to Fourier synthesis from an incomplete finite-resolution set of coefficients.

A second approach, which is not subject to the limitations imposed by the choice of a parameterized model of the density, is the maximum-entropy (also abbreviated MaxEnt) method. The appeal of the method is evident when counting the increasing number of applications to charge-density studies that have appeared in the crystallographic literature in the last ten years: see among the most recent ones Restori & Schwarzenbach (1995), Papoular *et al.* (1996), Takata & Sakata (1996), and Yamamoto *et al.* (1996), and the works cited in relevant sections of reviews on charge-density studies (Spackman & Brown, 1994) and on maximum-entropy methods in crystallography (Gilmore, 1996). In principle, MaxEnt maps are not tied to any particular multipolar expansion or radial deformation function and can mirror any degree of angular and radial deformation that is present in the observations.

All of the studies published so far have been aiming at the reconstruction of the total electron density in the crystal by redistribution of all electrons, under the constraints imposed by the maximum-entropy requirement and the experimental data.† The authors usually invoke the maximum-entropy principle of Jaynes (1957*a*,*b*, 1968, 1983), although the underlying connection with the structural model, known as the *random scatterer model*, is seldom explicitly mentioned.

According to the latter model, the crystal is described as formed of a number of equal scatterers, all randomly, identically and independently distributed. This simplified picture, and the interpretation of the electron density in terms of a positional probability distribution to generate a statistical ensemble of structures, lead to the selection of the map having maximum relative entropy with respect to some *prior-prejudice* distribution $m(\mathbf{x})$ (Bricogne, 1984, 1988*a*, 1991*c*).

When it is used to specify an ensemble of random structures, in the sense mentioned above, the MaxEnt distribution of scatterers is the one that rules out the smallest number of structures, while at the same time reproducing the experimental observations for the structure-factor amplitudes as expectation values over the ensemble. Thus, provided that the random scatterer model is adequate, deviations from the prior prejudice (see below) are enforced by the fit to the experimental data, while the maximum-entropy principle ensures that no unwarranted detail is introduced. This seemingly compelling justification for MaxEnt must however be subjected to careful scrutiny, as will now be performed.

2.3. *Test studies with the MaxEnt method*

Since 1993, a number of studies have been devoted to assessing the limitations of the maximum-entropy method when applied to charge-density studies, especially in conjunction with uniform prior-prejudice distributions. We summarize here the main points that have arisen from these model studies:

(i) *Uneven distributions of residuals*. The MaxEnt calculations in the presence of an overall χ^2 constraint suffer from highly nonuniform distributions of residuals, first reported and discussed by Jauch & Palmer (Jauch & Palmer, 1993; Jauch, 1994); the error accumulates on a few strong reflections at low resolution. The phenomenon is only partially cured by devising an *ad hoc* weighting scheme (de Vries *et al.*, 1994; Iversen *et al.*, 1995; Yamamoto *et al.*, 1996). Carvalho *et al.* (1996) have discussed this topic, and suggested that the recourse to as many constraints as degrees of freedom would cure the problem.

(ii) *Dynamic range of the density and low-density regions in the crystal*. In their work cited above, Jauch & Palmer first pointed out the inadequacies of the method in dealing with densities having a large dynamic range. Additional evidence of these inadequacies has come

† After acceptance of this paper, the authors became aware of valence-only MaxEnt reconstructions contained in the doctoral thesis of Garry Smith (1997).

from Papoular, Vekhter & Coppens, who worked on observed and simulated data sets for α-glycine (Papoular *et al.*, 1996). In the latter study, when all electrons were redistributed with a single-channel approach, the density of the H atoms was clearly flattened and features below $2\ \mathrm{e\ \AA^{-3}}$ were in general deemed to be scarcely significant because the large dynamic range of the total density reduced the sensitivity level. A two-channel calculation,† fitting structure factors calculated from the deformation density, did not suffer from the same limitations owing to the reduced dynamic range of the density to be reconstructed.

Errors in the low-density regions of the crystal were also found in a MaxEnt study on noise-free amplitudes for crystalline silicon by de Vries, Briels, Feil, te Velde & Baerends (1996). Data were fitted exactly, by imposing a standard uncertainty of 5×10^{-4} on the synthetic structure-factor amplitudes. The authors demonstrated that artificial detail was created at the midpoint between the Si atoms when all the electrons were redistributed with a uniform prior prejudice; extension of the resolution from the experimental limit of 0.479 to 0.294 Å could decrease the amount of spurious detail but did not reproduce the value of the reflection $F(222)$, which had been left out of the data set fitted.

(iii) *Dependence of results on the prior-prejudice distribution*. Nonuniform prior-prejudice distributions (NUP for short in what follows) were initially introduced by Jauch & Palmer by centring three-dimensional Gaussian functions at the nuclear positions (Jauch & Palmer, 1993). These authors found that the low-density regions of the crystal changed significantly upon introduction of the nonuniform prior prejudice, but the uneven distribution of errors persisted.

Iversen *et al.* in their MaxEnt study of crystalline beryllium were the first to make use of nonuniform prior-prejudice distributions calculated by superposition of thermally smeared spherical atoms. More recently, a superposition of thermally smeared spherical atoms was used as NUP in model studies on noise-free structure-factor amplitudes for crystalline silicon and beryllium by de Vries, Briels & Feil (1996) The artefacts present in the densities computed with a uniform prior-prejudice distribution were shown to disappear upon introduction of the nonuniform prior prejudice, but no quantitative measure of the residual errors was given.

Finally, recent work of Iversen, Jensen & Danielsen, (1997) has carefully examined the bias associated with the accumulation of the error on low-order reflections and attempted a correction of the MaxEnt density. The study, based on a number of noisy data sets generated with Monte Carlo simulations, has produced a less nonuniform distribution of residuals and has given a quantitative estimate of the bias introduced by the uniform prior prejudice.

† Two-channel MaxEnt techniques have also been used in the study of magnetization and spin densities (Papoular & Gillon, 1990; Zheludev *et al.*, 1995) and to interpret unpolarized neutron diffraction data (Sakata *et al.*, 1993).

3. The Bayesian viewpoint on charge-density studies

None of the studies mentioned in §2 has explicitly addressed the main issue of the redistribution of core-electron densities under maximum-entropy requirements in the absence of high-resolution observations. This is indeed the key to explaining the unsatisfactory behaviour encountered so far in the applications of the method to charge-density studies.

The maximum-entropy method is qualitatively correct only when used as a method of evaluation of the joint probability distribution of structure factors, *i.e.* when it is equivalent to using the saddlepoint method (Bricogne, 1984). The assumption of large numbers of identical and independently distributed random increments is vital (only under this assumption can one derive combinatorial multiplicities that have the form of multinomial coefficients, from which the connection with entropy follows by Stirling's approximation). Trouble will follow whenever the maximum-entropy method is used as a magical regularizing or extrapolating device in situations where this assumption is devoid of physical justification.

3.1. *Maximum entropy and joint probability distributions of structure factors.*

In the context of macromolecular structure determination, the maximum-entropy method has been used as part of a procedure to calculate joint probabilities of structure factors from statistical models in which:

(*a*) as much as possible of the prior knowledge of the structure is incorporated;

(*b*) the rest is describable as being made up of other random constituents, distributed in a way for which an initial guess is available, but for which a better model is to be built by forcing a tighter fit to the observations.

The maximum-entropy method (*i.e.* the saddlepoint method) is excellent at giving good values of these joint probabilities and of conditional probabilities because it is being used in its natural context. It cannot be expected to give an unbiased final answer because by its very essence it knows no chemistry (*i.e.* the atoms or electrons or other 'gremlins' are assumed to be independent).

The way to proceed towards a sensible answer with the maximum-entropy method is to use the joint and conditional probabilities it is so good at calculating to test various hypotheses against one another, by means of likelihood criteria calculated from these distributions. Typically, we test a hypothesis (H1) against a null hypothesis (H0). Hypothesis H1 stipulates that the structure consists of a particular (physically or chemically correct) substructure, with the rest of the atoms or

electrons distributed randomly and independently of each other; while the null hypothesis (H0) stipulates that all the atoms (including those of the putative substructure) are randomly distributed.

The distributions of random constituents are only allowed to be as nonuniform as is strictly necessary to produce the desired degree of fit to the observations, since they are built by the maximum-entropy method. The latter is also used to deduce the characteristics of the implied joint distributions of structure factors from which likelihoods are calculated (Bricogne, 1988*a*, 1991*c*).

In the scheme outlined above, the maximum-entropy method is used only to do what it does best, namely handle random distributions of a large number of independent constituents (the physics-free or chemistry-free part of the model at each stage of the guessing game). A physically or chemically valid interpretation of the data is thus extracted by sequentially testing hypotheses, the likelihoods of which involve the maximum-entropy method in the description of the still-random part of the model. The claims of the maximum-entropists that the MaxEnt reconstruction of electron density always gives a universal bias-free intermediate, from which all relevant hypotheses can be subsequently tested, are not to be believed.

3.2. *The joint use of ME distributions and structural models*

If any prior knowledge that could be put in the prior prejudice is withheld, the maximum-entropy results cannot be expected to reproduce it, since it represents improbable collusions between supposedly independent 'gremlins' which the ME method is precisely designed to rule out. Unphysical prior-prejudice distributions can bias maximum-entropy maps by building into them too much ignorance, which often cannot be cured by the limited information contained in the observations; one must use the method only when this ignorance has been minimized in a genuine fashion.

For these reasons, substructures that scatter well beyond the experimental resolution should be left out of the subset of scatterers distributed at random. The data sets commonly collected for charge-density studies rarely extend beyond 0.4 Å resolution, but scattering from the atomic core does extend well beyond this limit†.

† When in-house low-temperature studies are performed, the maximum resolution is imposed by data-collection geometry and fall-off of the scattered intensities below the noise level, rather than by negligible high-resolution structure-factor amplitudes. Use of Ag $K\alpha$ radiation would for example allow measurement of diffracted intensities up to 0.35 Å for amino acid crystals below 30 K (Destro, 1998). Similarly, model calculations show that noise-free structure factors computed from atomic core electrons would be still nonzero up to 0.1 Å. The use of synchrotron radiation is likely to allow accurate high-order data measurements that enable the study of atomic core deformations.

It is therefore clear that MaxEnt redistribution of all electrons, using a uniform prior prejudice and carried out in the absence of very high resolution diffraction measurements, cannot be expected to reproduce a physically acceptable picture of atomic cores. The reconstruction of total electron densities from limited-resolution diffraction measurements amounts to a misuse of the maximum-entropy method, especially when the prior prejudice is uniform. Any experimental uncertainty in the observations used as constraints will be taken advantage of by the maximum-entropy method to spread the electrons more evenly than they really are by virtue of the quantum laws governing atomic structure. In a sense, one is asking too much from the observations (*i.e.* to tell one that the crystal is made up of atoms and that bonds of different strength and nature are present in between atoms) from too poor an initial guess (*i.e.* that the electrons might well be spread out evenly everywhere in the cell without interacting).

The multichannel Bayesian formalism is not restricted to handling all components of a model exclusively through the ME method. The contribution from the core electrons, which is not completely defined from the diffraction data alone, but about which knowledge is available from other sources (*e.g.* quantum mechanics), should be treated through a conventional parameterized model. The contribution from the valence electrons, on the other hand, can be described in terms of a distribution of electrons for which a sensible prior prejudice $m(\mathbf{x})$ can be provided on the basis of a null hypothesis (*e.g.* a valence procrystal). To this prior prejudice some 'minimal readjustment' must be applied to fit the observations. This valence component is therefore amenable to a ME treatment.

More subtle prior knowledge that cannot be put into the prior-prejudice distribution concerns 'stereochemistry', or more generally specific rules governing local structure that violate the assumption of independence. This is where the sequential inference procedure described above takes over, the maximum-entropy method being used only on the unstructured ('random') part of the model.

This computational strategy would be the analogue of detecting stereochemically correct fragments and optimizing their placement during a crystal structure solution. The maximum-likelihood refinement of those multipolar parameters is superior to least-squares refinement in that it is capable of taking into account a rather elaborate description of the causes of the current discrepancies from the observations, namely a possibly rather complicated mixture of nonuniformly distributed 'gremlins' that have not yet been fully identified; this is considerably more versatile than a least-squares residual based purely on experimental errors or even on propagation of errors in the model parameters.

The structured approach outlined above extends the methodology of crystal-structure determination to the atoms themselves, with quantum-mechanically based functional parameterizations playing the role of databases of chemically correct fragments.

3.3. *The ME equations and density: a brief reminder*

The general computational mechanism of Bayesian crystal-structure determination in the presence of various sources of partial phase information was first outlined by Bricogne (1988*a*); a status report, now somewhat dated, about its actual implementation for a number of crystallographic problems was given by the same author (Bricogne, 1993*a*).

In this brief expository section, we recall the maximum-entropy equations and the functional form of the ME probability distribution, mostly to introduce the terminology and notation which will be used in §4.2 and in Appendix *A* to discuss the crucial issues of sampling and aliasing. The formulation is the one obtainable for randomly and independently distributed electrons [whose prior-prejudice probability distribution will be denoted as $m(\mathbf{x})$], in the presence of a subset of electrons whose distribution is assumed to be known. The latter structure will be denoted as '*fragment*'.

Let us consider a collection $H = (\mathbf{h}_1, \mathbf{h}_2, \ldots, \mathbf{h}_M)$ of symmetry-unique reflections. We denote by $\mathbf{F}^*_{\mathbf{h}_j}$ the 'target' phased structure-factor amplitude for reflection $\mathbf{h}_j$ and by $\mathbf{F}^{\rm frag}_{\mathbf{h}_j}$ the contribution from the known substructure to the structure factor for the same reflection. We are interested in a distribution of electrons $q(\mathbf{x})$ that reproduces these target phased amplitudes, in the sense that, for each structure factor in the set of observations H,

$$\mathbf{F}^*_{\mathbf{h}_j} = \mathbf{F}^{\rm frag}_{\mathbf{h}_j} + \mathbf{F}^{\rm rand}_{\mathbf{h}_j}, \tag{1}$$

where the contribution $\mathbf{F}^{\rm rand}_{\mathbf{h}_j}$ of the random scatterers is related to $q(\mathbf{x})$ by

$$\mathbf{F}^{\rm rand}_{\mathbf{h}_j} = nf|G| \int_V q(\mathbf{x}) \exp(2\pi i \mathbf{h}_j \cdot \mathbf{x})\, {\rm d}^3\mathbf{x}. \tag{2}$$

In this expression, $|G|$ is the number of elements of the space group of the crystal and f and n are the scattering power and number of the random scatterers in the asymmetric unit, respectively.

Since all the scatterers are identical, their structure factors can be normalized to unitary structure factors, as is always the case for homogeneous structures of normal scatterers (Bricogne, 1988*a*):

$$\mathbf{U}^{\rm rand}_{\mathbf{h}_j} = \mathbf{F}^{\rm rand}_{\mathbf{h}_j}/(nf|G|) = (\mathbf{F}^*_{\mathbf{h}_j} - \mathbf{F}^{\rm frag}_{\mathbf{h}_j})/(nf|G|). \tag{3}$$

Now we make use of the invariance of $q(\mathbf{x})$ under symmetry operations of space group G:

$$q(\mathbf{x}) = (1/|G|) \sum_{g\in G} q(\mathbf{R}_g\mathbf{x} + \mathbf{t}_g) \tag{4}$$

and of the group structure of G, to rewrite equation (2) as

$$\mathbf{U}^{\rm rand}_{\mathbf{h}_j} = \int_V q(\mathbf{x}) \left\{ (1/|G|) \sum_{g\in G} \exp[2\pi i \mathbf{h}_j \cdot (\mathbf{R}_g\mathbf{x} + \mathbf{t}_g)] \right\} {\rm d}^3\mathbf{x}. \tag{5}$$

The quantity in curly brackets in equation (5) is called the *constraint function* $C_j(\mathbf{x})$.

To deal with all the observations $\mathbf{h}_j \in H$ in compact form, the unitary structure-factor components can be arranged in a vector $\mathbf{U}^{\rm rand}$ and the components of the constraint functions collected in a vector $\mathbf{C}(\mathbf{x})$. The ME distribution of electrons $q^{\rm ME}(\mathbf{x})$ then takes the form (Jaynes, 1957*a*, 1968)

$$q^{\rm ME}(\mathbf{x};\, \boldsymbol{\lambda}^*) = [m(\mathbf{x})/Z(\boldsymbol{\lambda}^*)] \exp[\boldsymbol{\lambda}^* \cdot \mathbf{C}(\mathbf{x})], \tag{6}$$

where $Z(\boldsymbol{\lambda})$ is a normalizing factor for $q(\mathbf{x})$:

$$Z(\boldsymbol{\lambda}) = \int_V m(\mathbf{x}) \exp[\boldsymbol{\lambda} \cdot \mathbf{C}(\mathbf{x})]\, {\rm d}^3\mathbf{x} \tag{7}$$

and the saddlepoint $\boldsymbol{\lambda} = \boldsymbol{\lambda}^*$ is computed by solving the maximum-entropy equations:

$$\nabla_{\boldsymbol{\lambda}} (\log Z(\boldsymbol{\lambda})) = \mathbf{U}^{\rm rand}. \tag{8}$$

The name of the distribution is due to the fact that the saddlepoint $\boldsymbol{\lambda}^*$ can also be obtained as the vector of Lagrange multipliers needed to find the distribution $q = q^{\rm ME}$ for which the relative entropy $\mathcal{S}_m$,

$$\mathcal{S}_m(q) = -\int_V q(\mathbf{x}) \log[q(\mathbf{x})/m(\mathbf{x})]\, {\rm d}^3\mathbf{x}, \tag{9}$$

is at a maximum (see Bricogne, 1984, and references therein).

4. The rôle of the prior-prejudice distribution

It appears from formula (5) that the prior-prejudice distribution $m(\mathbf{x})$ is a fundamental quantity in the calculation of the ME distribution of electrons, in that the latter is obtained by *modulation of* $m(\mathbf{x})$. In all those regions where the modulating factor required to fit the observations is unity, the final picture is therefore always going to coincide with the prior expectation itself. For this reason, it is of the greatest importance that some of the prior information available about the system under study be conveyed into the calculation by means of a sensible choice for the prior-prejudice distribution.

This is especially true when the observations are not informative enough, as is the case for total charge-density reconstruction based on finite-resolution X-ray diffraction data. Even when valence electrons only are redistributed at random, the shell structure of the atomic densities might still require high-order components that are past the experimental resolution (Lu *et al.*, 1993). The choice of the uniform prior-prejudice distribution amounts to ignoring the presence of atoms in the crystal

so that its property of being 'maximally noncommittal' is no longer a virtue but a vice: it is in fact *too* noncommittal, because prior knowledge which will later be used to criticize the results has not been made available to the ME calculation.

Not only is the choice of a uniform prior-prejudice distribution not sensible; it also exposes the calculation to two main sources of computational errors, both connected with the functional form of the ME distribution of scatterers, and with its numerical evaluation: namely series-termination ripples and aliasing errors in the numerical sampling of the exponential modulation of $m(\mathbf{x})$. The next two sections will illustrate these two essential points in some detail.

4.1. *The spectrum of the exponential modulation of $m(\mathbf{x})$*

As already pointed out by Jauch (1994), the series appearing in the exponential factor that modulates $m(\mathbf{x})$ in equation (5) has a finite number of terms and can therefore give rise to series-termination artefacts. In particular, although the exponentiation will ensure positivity of the resulting density, series-termination ripples will be present in the reconstructed map whenever the spectrum of the modulation required by the observations extends significantly past the resolution of the series appearing in the exponential. This in turn will depend both on the 'true' density whose Fourier coefficients are being fitted and on the choice for the prior prejudice.

The phenomenon can be illustrated by considering a model density $q(\mathbf{x})$ from which diffraction data can be computed at arbitrarily high resolution. The (normalized) exponential factor needed to reconstruct $q(\mathbf{x})$ by ME modulation of a chosen prior-prejudice distribution $m(\mathbf{x})$ can be written

$$[1/Z(\boldsymbol{\lambda})]\exp[\boldsymbol{\lambda}\cdot\mathbf{C}(\mathbf{x})] = q(\mathbf{x})/m(\mathbf{x}). \qquad (10)$$

The series in the exponential is called ω: $\omega(\mathbf{x}) = \boldsymbol{\lambda}\cdot\mathbf{C}(\mathbf{x})$.

Fourier analysis of the logarithm of the ratio $q(\mathbf{x})/m(\mathbf{x})$ can now inform us about the extent to which the finite resolution of the observations fitted is likely to affect the ME reconstruction, depending on the choice for the prior prejudice. The better a guess $m(\mathbf{x})$ is, the smaller the amplitudes of the Lagrange multipliers will be. Finite-resolution effects will be negligible when the use of a good nonuniform prior prejudice keeps the size of the Lagrange multipliers to a minimum.

Fig. 1 shows the average strength of the Fourier coefficients of $\log[q(\mathbf{x})/m(\mathbf{x})]$, with $q(\mathbf{x})$ a multipolar synthetic density for α-glycine at 23 K and two different prior-prejudice distributions $m(\mathbf{x})$. It is clear that the exponential needed to modulate the uniform prior still has Fourier coefficients larger than 0.01 past the experimental resolution limit of 0.436 Å. Any attempt at fitting the corresponding experimental structure-factor amplitudes by modulation of the *uniform* prior-prejudice distribution will therefore create series-termination ripples in the resulting ME distribution.

The exact amount of error introduced cannot immediately be inferred from the strength of the amplitudes of the neglected Fourier coefficients because errors will pile up in different points in the crystal depending on the structure-factor phases as well; to investigate the errors, a direct comparison can be made in real space between the ME map and a map computed from exponentiation of a resolution-truncated 'perfect' ω map, whose Fourier coefficients are known up to any order by analysing $\log[q(\mathbf{x})/m(\mathbf{x})]$.

In particular, if the ω map suffers from an error $\Delta\omega$ due to its finite resolution:

$$\omega^{\text{model}}(\mathbf{x}) = \boldsymbol{\lambda}\cdot\mathbf{C}(\mathbf{x}) + \Delta\omega(\mathbf{x}), \qquad (11)$$

$$\begin{aligned} q^{\text{model}}(\mathbf{x}) &= q(\mathbf{x}) + \Delta q(\mathbf{x}) \\ &= [m(\mathbf{x})/Z(\boldsymbol{\lambda})]\exp[\omega(\mathbf{x}) + \Delta\omega(\mathbf{x})], \end{aligned} \qquad (12)$$

the error in the final ME map will be proportional to the density itself:

$$\Delta q(\mathbf{x}) = q(\mathbf{x})\{\exp[\Delta\omega(\mathbf{x})] - 1\} \approx q(\mathbf{x})\Delta\omega(\mathbf{x}) \qquad (13)$$

for $\Delta\omega(\mathbf{x}) \ll 1$. Errors are therefore enhanced in high-density regions.

4.1.1. *α-Glycine ME valence density from noise-free data*. To check this prediction, a number of ME charge-density calculations have been performed with the computer program *BUSTER* (Bricogne, 1993*a*) on a set of synthetic structure factors for a crystal of α-glycine at 23 K. A multipolar fit up to the hexadecapolar level was carried out with the computer program *VALRAY*

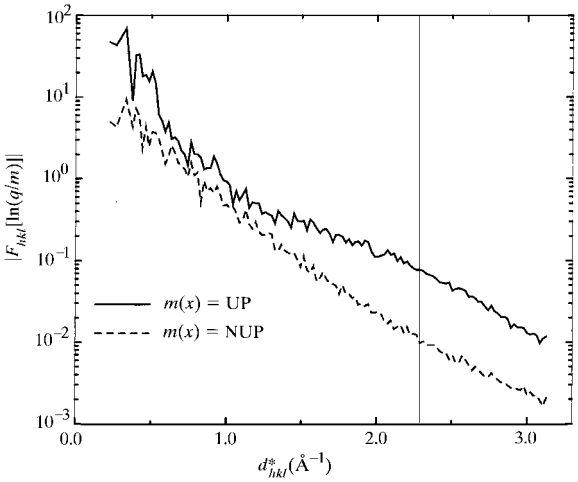

Fig. 1. Amplitudes of the Fourier coefficients of $\log[q(\mathbf{x})/m(\mathbf{x})]$ in resolution bins for α-glycine at 23 K. $q(\mathbf{x})$: total model density from a multipolar fit to 23 K diffraction data (Destro, 1998). Solid line: $m(\mathbf{x})$ uniform distribution. Dashed line: $m(\mathbf{x})$ core and valence monopoles. The vertical bar marks the experimental resolution limit 0.436 Å.

(Stewart & Spackman, 1983) against a set of 3822 experimental structure-factor amplitudes up to 0.436 Å resolution (Destro, 1998); a set of 1500 synthetic structure factors,† complete up to a resolution of 0.582 Å, was calculated from the resulting multipolar expansion $q_{\rm tot}^{\rm model}(\mathbf{x})$.

The ME valence density for α-glycine has been calculated targeting the multipolar structure-factor phases as well as the amplitudes (the space group of the structure is centrosymmetric, $P2_1/n$). The core density has been kept fixed to a superposition of atomic core densities; for those runs that used a nonuniform prior-prejudice distribution $m(\mathbf{x})$, the latter was computed from the superposition of atomic valence-shell monopoles $q_{\rm val}^{\rm IAM}(\mathbf{x})$; both core and valence monopole functions are those of Clementi (1965), localized by Stewart (1980); the positional, displacement and electronic population parameters used for the fragment and NUP procrystal densities were those of the multipolar model from which the data were calculated. Further details about the computational strategy are found in §5.

The dynamic range of the α-glycine model valence density at this temperature is $\sim$2500; this fairly high value is mainly due to the sharp increase of the valence monopole functions of O atoms at approximately 0.196 Å from the nucleus, and to the presence of low-density intermolecular regions (the minimum for this model density is 0.0024 e Å^{-3}).

(i) *Uniform prior prejudice*. Fig. 2(*a*) shows the model deformation density in the plane of the carboxylate moiety. Fig. 2(*c*) shows the ME deformation density in the same plane, calculated from a ME distribution obtained from a uniform prior prejudice for the valence electrons; the deformation map has been calculated by subtracting from the ME map the procrystal valence density $q_{\rm val}^{\rm IAM}(\mathbf{x})$ after the *BUSTER* job had converged.

Already from the comparison between Figs. 2(*a*) and (*c*) it is apparent that the reconstruction is unsatisfactory; Fig. 3(*b*) shows the residual map, obtained by subtracting the model valence density from the ME map. The valence density is affected by errors up to 26% (around +1.7 e Å^{-3}, exceeding the largest contour level) around the O atoms.

To check for the origin of these errors, a 'perfect' valence ω map was computed from the model valence density; its spectrum was truncated at the same resolution used for the ME calculation; the valence ω map was then resynthesized from this resolution-truncated set of Fourier coefficients and exponentiated back. The valence residual map for this density is shown in Fig. 3(*c*); the errors around the O atoms in Figs. 3(*b*) and (*c*) have the same shape; this is a strong indication that these do indeed correspond to Fourier-truncation ripples in the valence ω map.

We stress here that any low-temperature valence density for a small organic molecule will have a comparably high dynamic range so that even valence-only ME studies will always be likely to need a nonuniform prior prejudice if truncation ripples are to be avoided.

(ii) *Nonuniform prior prejudice*. Fig. 2(*b*) shows the ME deformation density [see formula (26)] in the carboxylate plane of α-glycine, from a *BUSTER* calculation that used a nonuniform prior prejudice of thermally smeared valence monopoles.

The dynamic range of the exp(ω) map is reduced to a value of $\sim$14 when a nonuniform prior prejudice of spherical valence monopoles is used: as a consequence, the size of the Lagrange multipliers is reduced by between one and two orders of magnitude and the error due to series truncation in the ω map is less than 0.2 e Å^{-3} in absolute value everywhere in the cell (Fig. 3*a*), the r.m.s. deviation from the model being as low as 0.01 e Å^{-3}.‡

4.2. *Numerical sampling of the exponential modulation of m(**x**)*

A second major source of computational difficulties associated with uniform prior-prejudice distributions is connected with the extremely fine sampling grids that are needed to avoid aliasing effects (Brigham, 1974) in the numerical Fourier synthesis of the modulating factor in (5). To predict the dependence of aliasing effects upon the prior prejudice, we need to examine more closely the way the ME distribution of scatterers is actually synthesized from the values of the Lagrange multipliers $\boldsymbol{\lambda}$. We recall that an equivalent analysis was carried out by Bricogne (1984, Section 3) to illustrate the phase extrapolation power of exponential modelling in the context of direct methods.

First, we rewrite the constraint functions appearing in the observational equations (5) so as to separate the effects of the amplitude and of the phase of the residual target structure factor:

$$\mathbf{U}_{\mathbf{h}_j}^{\rm rand} = \left|\mathbf{U}_{\mathbf{h}_j}^{\rm rand}\right| \exp(i\varphi_j). \qquad (14)$$

Multiplication of the observational equations (5) by a factor $\exp(-i\varphi_j)$ leads to the modified constraint functions:

† The choice of the number of reflections was dictated by the limited number of observational constraints that can be handled when solving the MaxEnt equations by means of the duality algorithm; the more recent implementation of a different algorithm that handles measurement errors (Roversi *et al.*, 1998) has now allowed *BUSTER* to deal with up to 10 000 independent diffraction amplitudes.

‡ The value of the r.m.s. deviation from the reference density can be deceptively low because in the intermolecular regions the model density is virtually the same as the one made of spherical-valence shells, which was used as a nonuniform prior prejudice. The agreement between the ME map and the reference model is very close in those regions.

$$C'_j(\mathbf{x}) = (1/|G|) \sum_{g\in G} \exp[2\pi i \mathbf{h}_j \cdot (\mathbf{R}_g\mathbf{x} + \mathbf{t}_g) - i\varphi_j]. \quad (15)$$

Taking the real and imaginary parts of the left- and right-hand sides of the newly rewritten observational equations, one obtains:

$$\int_V q(\mathbf{x})\Re\{C'_j(\mathbf{x})\}\, \mathrm{d}^3\mathbf{x} = \left|\mathbf{U}^{\mathrm{rand}}_{\mathbf{h}_j}\right| \quad (16)$$

$$\int_V q(\mathbf{x})\Im\{C'_j(\mathbf{x})\}\, \mathrm{d}^3\mathbf{x} = 0. \quad (17)$$

Correspondingly, we introduce symbols for the amplitude κ_j and phase θ_j of each complex Lagrange multiplier λ_j: $\lambda_j = \kappa_j(\cos\theta_j + i\sin\theta_j)$.

With this choice of constraint function and Lagrange multiplier, we can rewrite formula (5) and express the ME distribution of electrons as:

$$q^{\mathrm{ME}}(\mathbf{x}) = [m(\mathbf{x})/Z(\boldsymbol{\kappa}, \boldsymbol{\theta})] \exp\left\{ \sum_j \kappa_j [\cos(\theta_j)\Re\{C'_j\} + \sin(\theta_j)\Im\{C'_j\}] \right\}. \quad (18)$$

The sum over symmetry operations in formula (15) can be rewritten by considering the effect of multiplying vector $\mathbf{h}_j$ by the rotation matrices $\mathbf{R}_g$. The collection of distinct reciprocal vectors $\mathbf{h}_j\mathbf{R}_g$ is called the *orbit* of reflection $\mathbf{h}_j$; Γ_j is the set of symmetry operations in G whose rotation matrices are needed to generate the orbit of $\mathbf{h}_j$; $|\Gamma_j|$ denotes the number of elements in the same orbit (Bricogne, 1993*b*).

The real part of the constraint function can be written

$$\begin{aligned}\Re\{C'_j\} &= (1/|G|) \sum_{g\in G} \cos[2\pi\mathbf{h}_j \cdot (\mathbf{R}_g\mathbf{x} + \mathbf{t}_g) - \varphi_j] \\ &= (1/|\Gamma_j|) \sum_{\gamma\in\Gamma_j} \cos[2\pi\mathbf{h}_j \cdot (\mathbf{R}_\gamma\mathbf{x} + \mathbf{t}_\gamma) - \varphi_j] \end{aligned} \quad (19)$$

and a similar expansion holds for the imaginary part.

Substitution of (19) within (18) gives

$$q^{\mathrm{ME}}(\mathbf{x}) = [m(\mathbf{x})/Z(\boldsymbol{\kappa}, \boldsymbol{\theta})] \exp\left\{ \sum_j^M \sum_{\gamma\in\Gamma_j} (\kappa_j/|\Gamma_j|) \times \cos[2\pi\mathbf{h}_j \cdot (\mathbf{R}_\gamma\mathbf{x} + \mathbf{t}_\gamma) - \psi_j] \right\}, \quad (20)$$

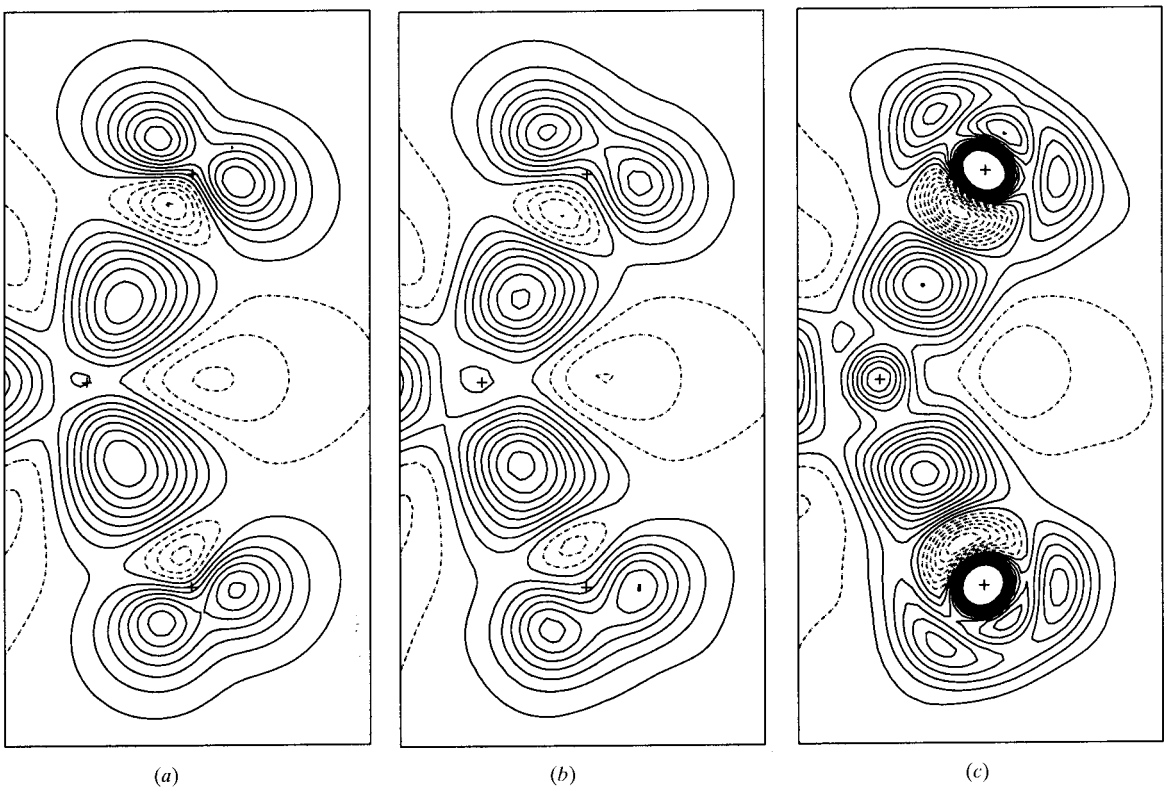

(*a*) (*b*) (*c*)

Fig. 2. α-Glycine. Dynamic valence deformation density in the COO^- plane. (*a*) $\Delta q^{\mathrm{model}}_{\mathrm{val}}(\mathbf{x})$: model dynamic valence deformation density. (*b*) $\Delta q^{\mathrm{ME}}_{\mathrm{NUP}}(\mathbf{x})$: maximum-entropy valence-deformation density [see formula (26)], obtained by modulating a nonuniform prior of spherical-valence shells: $m(\mathbf{x}) = q^{\mathrm{IAM}}_{\mathrm{val}}(\mathbf{x})$. (*c*) $q^{\mathrm{ME}}_{\mathrm{UP}}(\mathbf{x}) - q^{\mathrm{IAM}}_{\mathrm{val}}(\mathbf{x})$: deformation density computed by subtracting the spherical valence-shell density from the maximum-entropy valence map calculated with a uniform prior. Map size: 2.0 × 4.0 Å. Contour levels: from −1.0 to 1.0 e Å^{-3}, step 0.075 e Å^{-3}, dashed negative contours, zero contour omitted. Crosses indicate nuclear positions of the atoms defining the section.

where $\psi_j = \varphi_j + \theta_j$. This is the actual formula to compute the ME distribution by numerical Fourier synthesis followed by exponentiation. As with all Fourier series, aliasing errors can occur when the Fourier coefficients extend very far into reciprocal space if the grid upon which the density is sampled is not fine enough (Bricogne, 1993*b*).

To assess the extent to which the *exponentiated* Fourier series has appreciable Fourier amplitudes, and set the sampling grid accordingly, further development of formula (20) is needed. We first rewrite

$$q^{\mathrm{ME}}(\mathbf{x}) = [m(\mathbf{x})/Z(\boldsymbol{\kappa}, \boldsymbol{\theta})] \prod_{j=1}^{M} \prod_{\gamma \in \Gamma_j} \exp\{(\kappa_j/|\Gamma_j|) \times \cos[2\pi \mathbf{h}_j \cdot (\mathbf{R}_\gamma \mathbf{x} + \mathbf{t}_\gamma) - \psi_j]\}. \quad (21)$$

Expanding each of the exponential factors in a series of modified Bessel functions, the ME distribution can be written

$$q^{\mathrm{ME}}(\mathbf{x}) = [m(\mathbf{x})/Z(\boldsymbol{\kappa}, \boldsymbol{\theta})] \times \prod_{j=1}^{M} \prod_{\gamma \in \Gamma_j} \left(I_0(\kappa_j/|\Gamma_j|) + 2 \sum_{n=1}^{\infty} I_n(\kappa_j/|\Gamma_j|) \times \cos\{n[2\pi \mathbf{h}_j \cdot (\mathbf{R}_\gamma \mathbf{x} + \mathbf{t}_\gamma) - \psi_j]\} \right). \quad (22)$$

When the prior prejudice $m(\mathbf{x})$ is uniform, some of the Lagrange multiplier amplitudes are large (of the order of unity or greater). This is especially the case when sharp details are present in the density to be reconstructed and not in the prior prejudice chosen. For a given argument z, the ratio $I_n(z)/I_0(z)$ remains substantial until n exceeds z [see Fig. 4; the curve $I_n(z)/I_0(z)$ for $n = 1$ was also plotted in Bricogne (1984, Fig. 1)], so that large values of the Lagrange multiplier amplitudes $\boldsymbol{\kappa}$ will give rise to appreciable high-resolution coefficients in the Fourier series in (22).

This in turn will require very fine sampling grids along each crystallographic direction to avoid aliasing effects when the density is synthesized. The size of the arrays needed for the Fourier sampling of $q^{\mathrm{ME}}(\mathbf{x})$ would

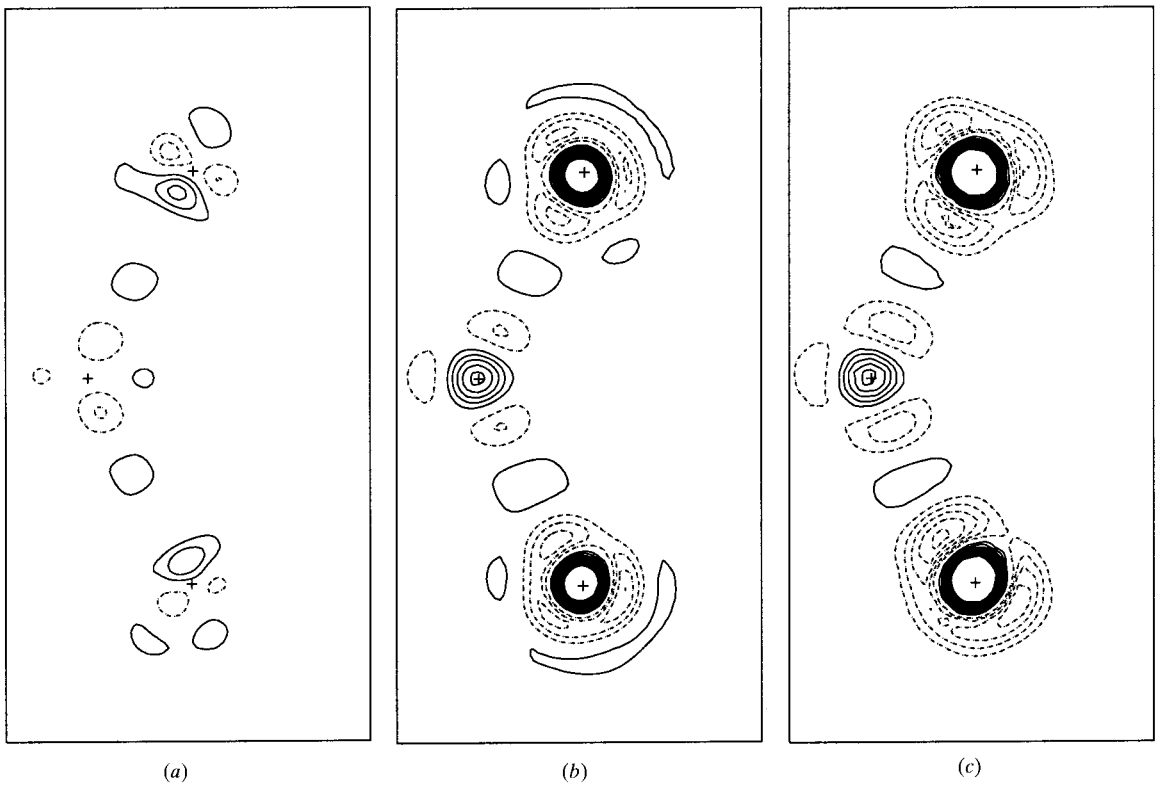

Fig. 3. α-Glycine. Valence residual dynamic density in the COO^- plane. (*a*) $q^{\mathrm{ME}}_{\mathrm{NUP}}(\mathbf{x}) - q^{\mathrm{model}}_{\mathrm{val}}(\mathbf{x})$: valence residual dynamic density for the maximum-entropy calculation with a nonuniform prior of spherical-valence shells. (*b*) $q^{\mathrm{ME}}_{\mathrm{UP}}(\mathbf{x}) - q^{\mathrm{model}}_{\mathrm{val}}(\mathbf{x})$: valence residual dynamic density for the maximum-entropy calculation with a uniform prior. (*c*) $\exp[\omega^{\mathrm{model}}_{0.582}(\mathbf{x})] - q^{\mathrm{model}}_{\mathrm{val}}(\mathbf{x})$: valence residual dynamic density obtained subtracting the valence model density from the exponentiated and 0.582 Å-truncated valence ω map (see text). Contour levels: from -1.0 to 1.0 e Å^{-3}; (*a*) step 0.05 e Å^{-3}; (*b*) and (*c*) step 0.10 e Å^{-3}. Dashed negative contours, zero contour omitted. Map size and orientation as in Fig. 2. Crosses indicate nuclear positions of the atoms defining the section.

therefore easily exceed ten million locations for all-electron runs on low-temperature structures. It is clear that ME distributions of scatterers that contain atomic cores, when obtained by modulation of a uniform prior prejudice, are bound to be spoiled by aliasing effects, unless allowance is made for prohibitively large amounts of memory space.

When the reconstruction of the density is carried out by modulation of a prior prejudice of spherical atoms, only the deformation features have to be accommodated; this can be accomplished relatively easily in that they are usually smooth so that the Lagrange multipliers are usually below 0.01 in modulus or even smaller for valence-only runs. No aliasing problems then occur in the synthesis of $q^{\mathrm{ME}}(\mathbf{x})$.

5. Computational mechanism

In this section, we examine more closely the actual computational mechanism that allows the calculation of ME distributions of electrons from high-resolution X-ray diffraction data, as implemented in the computer program *BUSTER*. The general structure of the program has been described by Bricogne (1993*a*); we therefore briefly recall here only those aspects that are relevant to the application to charge-density studies. In particular, the communication to *BUSTER* of various quantities calculated from subsets of electrons have been accomplished by means of an interface to the computer program *VALRAY* (Stewart & Spackman, 1983), thus making optimal use of the built-in capability of the multipolar formalism to partition atomic densities between core and valence contributions.

The first implementation described here is restricted to the case of absolute-scale noise-free diffraction data without anomalous-dispersion contributions. Attention will be confined to the construction of the ME distribution of scatterers based on a set of experimental amplitudes, the trial phases attached to them and the currently available prior information. Phase hypothesis generation and maximum-likelihood refinement of phases, especially important to adequately treat noncentrosymmetric structures, will be dealt with in a subsequent paper.

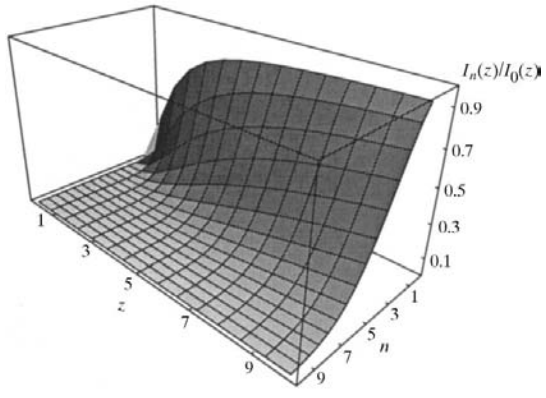

Fig. 4. Ratio $I_n(z)/I_0(z)$.

5.1. *Data preparation and incorporation of prior information*

5.1.1. *Initialization stage*. Observed values $|\mathbf{F}^*|$ for the structure-factor amplitudes on an absolute scale are read together with the estimates for their error variances and with target values for the phases. The latter are encoded in Hendrickson–Lattman phase probability coefficients (Hendrickson & Lattman, 1970), which will make it possible to deal with acentric structures.

The number n of random scatterers in the asymmetric unit is declared in the input together with their scattering power f. When a fragment of core electrons is present, the number of scatterers in the random part and the number of scatterers in the fragment must consistently add up to the total number of electrons in the asymmetric unit. We notice that, because of the total scattering power nf intervening in the calculation of the target unitary structure-factor components in equations (3), there is a degree of freedom in the choice of the actual number of random scatterers. An estimation of the optimal number of scatterers should indeed be possible based on the log-likelihood gain (Bricogne, 1988*a*,*b*; Bricogne & Gilmore, 1990) and will indeed be crucial once the optimal handling of experimental error variances in the fit against noisy data is implemented.

5.1.2. *The fragment*. The distribution of electrons, if any, that is chosen as a known partial structure is described in terms of a list of N_{frag} atoms in the asymmetric unit; for each atom, the positional and displacement parameters $\mathbf{x}_j$ and $\boldsymbol{\beta}_j$ are given, together with the appropriate localized core-density functions $\rho_j^{\mathrm{core}}(|\mathbf{x}-\mathbf{x}_j|)$ (Stewart, 1980) and the corresponding core-electronic population coefficients P_j^{core}:

$$q^{\mathrm{frag}}(\mathbf{x}) \propto \sum_{j=l}^{N_{\mathrm{frag}}} [P_j^{\mathrm{core}} \rho_j^{\mathrm{core}}(|\mathbf{x}-\mathbf{x}_j|)] * Q_j(\mathbf{x}-\mathbf{x}_j;\boldsymbol{\beta}_j), \quad (23)$$

where Q_j is the (possibly anharmonic) probability density function used to thermally smear the atomic density. The multiplicity-weighted sum of the core population coefficients adds up to n_{frag}. At present, the model for the fragment substructure is rigidly fixed and the values of the parameters that appear in it are kept equal to those obtained by some multipolar model refined against suitable X-ray or neutron data; but in principle this restriction can be lifted and their values refined during the calculation.

5.1.3. *Data normalization and target structure-factor amplitudes*. If a fragment substructure has been specified, structure factors $\mathbf{F}^{\mathrm{frag}}$ are computed within *VALRAY* and read into *BUSTER*. The target values of

the unitary structure-factor components are calculated according to formula (3) and a suitable list of candidate reflections is selected from those within the resolution and $|E|^2$ thresholds (Bricogne, 1992, 1997) specified, for subsequent inclusion into the basis set (see §5.1.5)

5.1.4. *The nonuniform prior-prejudice distribution*. A nonuniform prior-prejudice distribution $m(\mathbf{x})$ for the random part of the structure can be specified in a similar fashion to that illustrated above for the fragment. A list of atoms contributing to the prior is declared with positional and displacement parameters together with the appropriate static atomic monopole density functions and electronic population parameters. In brief:

$$m(\mathbf{x}) \propto \sum_j \rho_j^{\rm mon}(\mathbf{x}; \mathbf{x}_j, \boldsymbol{\beta}_j, P_j^{\rm mon}).$$

All-electron runs described in the following section made use of a NUP of core- and valence-density functions, while valence monopoles only were used when computing ME distributions of valence electrons in the presence of core fragments.

The use of static monopole density functions that have no negative values (see Appendix *A*) ensure that $m(\mathbf{x})$ is positive everywhere in the asymmetric unit. Finally, we mention that, within the present implementation, aspherical atomic contributions could also be used to build other kinds of NUP (and/or fragments) simply by adding multipoles with $l > 0$, but a preliminary check would then be necessary in order to ensure the positivity of those distributions.

5.1.5. *Basis-set selection*. The elements of the Hessian matrix of $\log Z(\boldsymbol{\lambda})$ are computed from the appropriate expectation values of products of structure-factor components *via* structure-factor algebra (Bricogne, 1988*a*). At the outset, all Lagrange multipliers are zero and the Hessian is based on the prior-prejudice distribution only. Within *BUSTER*, the Hessian matrix is used to solve the maximum-entropy equations and to compute derivatives of the likelihood functions with respect to structure-factor components. These derivatives serve to choose the reflections whose presence in the basis set will maximize the sensitivity of the likelihood to the structural hypotheses, thus allowing for an optimal order of inclusion of new basis-set reflections along the lines described by Bricogne (1993*a*).

For the application described here, optimal basis-set selection will only be possible once the variances entering the likelihood function are on the scale of the experimental error variances. At the moment, the whole set of reflections greater than the $|\mathbf{E}|$ threshold and within the resolution range specified are fitted.

5.1.6. *Definition of the sampling grid*. The sampling grid for the calculation of the ME distribution depends on the data resolution and on the values of the Lagrange multipliers for the reflections, if an estimate for them is available, for example from some previous run on a subset of reflections. The grid is always chosen so as to minimize aliasing effects that can arise during the numerical synthesis of the prior-prejudice distribution and of the exponential factor modulating it, as discussed in §4.2.

Bandwidth of the prior-prejudice distribution. Thanks to the algorithm described in Appendix *A*, the prior-prejudice distribution can be sampled on arbitrary grids, so that in principle there would be no need to worry about its Fourier spectrum as far as generation of the ME distribution of scatterers in (20) is concerned. During the course of the calculation, $q(\mathbf{x})$ undergoes FFT, so that it is important to make sure that the grid chosen does not lead to severe aliasing errors due to undersampling of the prior prejudice.

A check on the bandwidth of the prior-prejudice distribution is performed by calculating the minimum value of the resolution $d^*_{\rm copy}$ for which the aliasing error:

$$\text{err} = \max\left[\frac{f_j(d^*_{\rm max})}{f_j\left(d^*_{\rm copy} - d^*_{\rm max}\right)}\right], \quad j = 1, N_{\rm at} \qquad (24)$$

is below the numeric threshold of 10^{-6}. The resolution $d^*_{\rm max}$ at which the aliasing error is computed is taken equal to the maximum resolution of the data set; the f_j are the dynamic atomic scattering factors used to compute the prior-prejudice distribution.

Bandwidth of the exponential modulating factor. A loop is performed on reflections in the basis set. For reflection $\mathbf{h}_j$, the smallest value of the index M for which

$$I_M(\kappa_j/|\Gamma_j|) \leq I_1(\kappa_j/|\Gamma_j|) \times 10^{-8} \qquad (25)$$

is found. The trial values of the Lagrange multiplier amplitudes κ_j are either estimated from the amplitude of the target structure factors, as explained by Bricogne (1984), or from some previous calculation. For the current reflection, M gives the maximum order of modified Bessel function that gives an appreciable contribution to the spectrum of the exponential modulation of $m(\mathbf{x})$ in (20). The process is repeated for all reflections.

The maximum value obtained for $d^*(M\mathbf{h}_j)$ is then used together with $d^*_{\rm copy}$ to define the grid according to the Shannon criterion (Bricogne, 1993*b*), based on a reciprocal radius $[d^*(M\mathbf{h}_j)_{\rm max} + d^*_{\rm copy}]$.

5.2. *Generation of the electron-density distribution*

5.2.1. *Solution of the ME equations*. The ME equations (8) are solved numerically for the Lagrange multipliers with the duality algorithm described by Bricogne (1991*a*). The starting values for the Lagrange multipliers are estimated from values at convergence of a previous run on a subset of the data, if this is available, or from the residual structure factors computed from the prior prejudice. The iterative procedure is stopped when the value of the relative lack of fit,

$$\text{L.o.f.} = \left\{ \left[\sum_i^{N_a+N_c} (\Re^2\{U_{i,\text{target}} - U_{i,\text{ME}}\} + \Im^2\{U_{i,\text{target}} - U_{i,\text{ME}}\}) \right] \times \left(\sum_i^{N_a+N_c} |U_{i,\text{target}}|^2 \right)^{-1} \right\}^{1/2},$$

reaches below the threshold 10^{-5}. Convergence is usually achieved in less than 50 cycles. When the constraints are given by the noisy data, a different algorithm is used which maximizes a 'Bayesian score' (Bricogne, 1993*a*; Roversi *et al.*, 1998).

5.2.2. *Total density reconstruction*. When a fragment is being used, the total density is reconstructed at the end of the calculation by sampling the dynamic density of the fragment $q^{\text{frag}}(\mathbf{x})$ on the same crystallographic grid used to compute $q^{ME}(\mathbf{x})$ and adding the two distributions

$$q^{\text{tot}}(\mathbf{x}) = \frac{nq^{ME}(\mathbf{x}) + n_{\text{frag}}q^{\text{frag}}(\mathbf{x})}{n + n_{\text{frag}}}. \qquad (26)$$

We mention here that, strictly speaking, the distributions obtained are positional probability distributions, which integrate to unity over the unit cell of the crystal. In the following sections, we shall refer to them as 'electron-density distributions', whose values in e Å^{-3} will be obtained by multiplying $q(\mathbf{x})$ by the nominal average density in the crystal $\langle\rho(\mathbf{x})\rangle$.

5.2.3. *ME deformation density maps*. Most of the relevant features of the charge-density distribution can be elegantly elucidated by means of the topological analysis of the total electron density (Bader, 1990); nevertheless, electron-density deformation maps are still a very effective tool in charge-density studies. This is especially true for all densities that are not specified *via* a multipole model and whose topological analysis has to be performed from numerical values on a grid.

Conventional implementations of the maximum-entropy method for charge-density studies do not allow easy access to deformation maps; a possible approach involves running a ME calculation on a set of data computed from a superposition of spherical atoms and subtracting this map from q^{ME} (Lecomte, 1995). Recourse to a two-channel formalism, which redistributes 'positive-' and 'negative-density' scatterers, fitting a set of difference Fourier coefficients, has also been made (Papoular *et al.*, 1996) but there is no consensus on what the definition of entropy should be in a two-channel situation (Bricogne, 1988*a*; Sakata *et al.*, 1993; Papoular *et al.*, 1996); moreover, the shapes and numbers of positive and negative scatterers may need to differ in a way that is difficult to specify.

Thanks to the particular choice made for the non-uniform prior prejudice, taken equal to a thermally smeared superposition of atomic shells, it is for the first time possible within the present approach to compute maximum-entropy deformation maps in a straightforward manner. Once the Lagrange multipliers $\boldsymbol{\lambda}$ have been obtained, the deformation density is simply

$$\Delta q^{\text{ME}}(\mathbf{x}) = m(\mathbf{x})\left\{\frac{\exp[\boldsymbol{\lambda}^* \cdot \mathbf{C}(\mathbf{x})]}{Z(\boldsymbol{\lambda}^*)} - 1\right\}. \qquad (27)$$

This map can have negative as well as positive features and yet its calculation involves only that of the positive map q^{ME}, thus providing a simpler alternative to the two-channel maximum-entropy approach mentioned above. First applications to noisy data (Roversi *et al.*, 1998) have confirmed the general usefulness of such ME deformation maps.

6. ME model studies on Si and Be

In this section, the capabilities of the method in reconstructing synthetic densities are tested under various choices for the prior-prejudice distribution, and/or core–valence partitioning scheme, on synthetic data computed from a model density. The use of synthetic data allows a comparison of the electron-density distribution obtained with the model density.

In the first part of the section, we describe the results of the first model studies performed with *BUSTER* on noise-free synthetic data sets for crystalline silicon and beryllium. Several experimental charge-density studies have been carried out for both silicon (Spackman, 1986; Lu & Zunger, 1992; Lu *et al.*, 1993) and beryllium (Stewart, 1977; Larsen & Hansen, 1984; Iversen *et al.*, 1995). In particular, the existence of *non-nuclear maxima* (NNM for short) in the electron-density distribution for these systems, suggested on the basis of theoretical (Zou & Bader, 1994) and experimental (Sakata & Sato, 1990; Takata *et al.*, 1994; Iversen *et al.*, 1995; Takata & Sakata, 1996) evidence, has been recently questioned (de Vries, Briels, Feil, te Velde & Baerends, 1996; de Vries, Briels & Feil, 1996).

6.1. *Silicon*

A multipolar density was computed for crystalline silicon by fitting the set of 30 structure-factor amplitudes measured by Saka & Kato (1986), plus the amplitude of the reflection $\mathbf{F}_{222}$ (Alkire *et al.*, 1982).† The space group is $Fd\bar{3}m$, origin choice 2: one Si atom in the asymmetric unit at site 8(*a*), $(\frac{1}{8}\frac{1}{8}\frac{1}{8})$; the multipolar refinement was performed with *VALRAY* (Stewart & Spackman, 1983). The model used is similar to the one described in Spackman (1986), except that no radial parameters were varied in our case: one isotropic displacement parameter was refined together with the electronic population

† We recall that $\mathbf{F}_{222}$ and other $h + k + l = 4n + 2$ reflections would be extinct ('forbidden') if the thermally smeared electron density of the Si atom had spherical symmetry.

parameters for the *L*- and *M*-shell monopoles, and for the symmetry-allowed deformation terms up to $l = 4$, namely one octopole and one hexadecapole. The monopole functions used are those of Clementi (1965), localized by Stewart (1980). Exponents in the radial deformation functions $r^n \exp(-\alpha r)$ of the higher poles were kept fixed to the values $n = 4$, $\alpha = 2.354$ a.u.$^{-1}$.

Scaled population parameters for *K*-, *L*- and *M*-shell monopoles at the end of refinement amounted to 2.07, 8.27 and 3.66 electrons, respectively. The isotropic displacement parameter was $U = 0.00561\,(3)$ Å^2. Statistical indices: $R(F) = 0.0019$, $wR(F) = 0.0016$, $R(F^2) = 0.0031$, $wR(F^2) = 0.0033$; G.o.f. = 13.00. Given the relative simplicity of the refinement performed, this is not the best possible model density for silicon but it was deemed to be good enough to be used as a reference, after a preliminary check on positivity of the valence density in the asymmetric unit (the maximum-entropy method would not reconstruct densities having negative values).

Model structure factors were computed from the multipolar model. Except where otherwise indicated, all calculations described in the following paragraphs used a set of 31 synthetic structure factors whose indices correspond to the ones of Saka & Kato (1986), plus the forbidden $\mathbf{F}_{222}$. This data set is not complete, as 20 reflections out of 51 within the experimental resolution limit of 0.479 Å are missing (but eight of the missing reflections are forbidden ones). A run performed against a data set complete up to 0.479 Å is described in §6.1.3.

The thermally smeared model electron density needed to check the quality of the ME reconstruction in real space was generated from the multipolar model, using the algorithm described in Appendix *A*, on the same grid used for the maximum-entropy calculation. Dynamic procrystal densities, used as nonuniform prior-prejudice distributions, were also generated from the same multipolar model, setting higher-pole population coefficients equal to zero. Plane (110) sections of the dynamic model electron density and of the all-electron monopole prior prejudice are shown in Figs. 5 and 6, respectively.

6.1.1. *Valence-only calculations*. The calculations described in this section were made by redistributing valence electrons in the random part and using a fragment of core electrons. All densities were computed on a $144 \times 144 \times 144$ grid. Table 2 reports some of the significant values of the total model density, together with the values obtained from the *BUSTER* runs. The *BUSTER* densities have been computed from the sum of the ME valence and model fragment distributions according to formula (26).

Two calculations have been performed using a fragment of *K*- and *L*-shell electrons and redistributing 3.66 electrons for the *M* shell. They differ only with respect to the prior-prejudice distribution. Calculation *A* used a NUP of *M*-shell valence monopoles, while calculation *B* used a uniform prior-prejudice distribution (UP). Both calculations successfully reconstruct the valence (and total) density; Figs. 7 and 8 report the error maps

$$\Delta q(\mathbf{x})^{\rm err} = \mathbf{q}^{\rm ME}(\mathbf{x}) - \mathbf{q}^{\rm model}(\mathbf{x})$$

in section (110) within the crystal. The error is lower than 0.05 e Å^{-3} in absolute value everywhere. Nuclear regions are less satisfactorily reconstructed; this is also a common problem in multipolar studies (Spackman, 1986; Howard *et al.*, 1995). The influence of the prior prejudice is in this case marginal, the dynamic range of the *M*-shell density being around 44.

Two runs using a fragment of *K*-shell core electrons redistributed *L*- and *M*-shell electrons in the random part. As was the case for *A* and *B*, these calculations only differ for the choice of the prior-prejudice distribution: *C* used a NUP of *L*- and *M*-shell monopoles, while *D* used a uniform prior prejudice. Larger errors are present in the nuclear region in the map for density *C*, Fig. 9. Even larger errors affect density *D* (Fig. 10).

6.1.2. *All-electron calculations*. From the calculations redistributing *L*- and *M*-shell electrons, it is already evident that even the use of a nonuniform prior-prejudice distribution cannot prevent errors as high as 0.2 e Å^{-3} from appearing in the reconstructed total density. All-electron runs, in which no fragment is used, are therefore expected to perform even worse; we stress that all the MaxEnt distributions obtained so far in the literature, with the exception of the two-channel deformation densities of Papoular *et al.* (1996), are precisely all-electron reconstructions. In particular, we reproduced here with calculation *E* the total density calculation with a NUP described by de Vries, Briels & Feil (1996); calculation *F*, using the UP, is equivalent to the ones described in Sakata & Sato (1990), Takata & Sakata (1996) and de Vries, Briels, Feil, te Velde & Baerends (1996) (compare maps in these papers with the one in Fig. 11).

As was expected, both *E* and *F* densities are heavily laden with artefacts. This is clearly visible in the error maps in Figs. 12 and 13. Density at the nuclear position is underestimated by about 28% (see Table 2), while series-termination ripples cluster around Si atoms in low-density regions. The series-termination ripples originating from atomic centres add up constructively between bonded atoms in density *F* to create a false NNM at position 16(*c*), the midpoint of the bond. The density profile along direction [111] in between bonded Si atoms is shown in Fig. 14. The value of the density at position 16(*c*) for calculation *F* is in excess of about 30%.

6.1.3. *Dependence of the results on resolution and data completeness*. The incompleteness of the Saka & Kato (1986) data set has been recently blamed for the unsatisfactory features of the ME reconstructions of the

Table 2. *Summary of BUSTER runs on model synthetic data for crystalline silicon*

Density	$24 \times n$†	$24 \times n_{frag}$‡	q_{max}	q_{min}	CC_{min}§	Δq^{err}_{max}¶	Δq^{err}_{min}
A	3.66 (NUP)	10.34	297.384	0.033	0.999	0.014	−0.049
B	3.66 (UP)	10.34	297.322	0.032	0.999	0.022	−0.112
C	11.93 (NUP)	2.07	297.576	0.032	0.999	0.142	−0.172
D	11.93 (UP)	2.07	304.168	0.023	0.999_5	6.734	−0.955
E	14 (NUP)	0	297.872	0.032	0.999	0.438	−0.200
F	14 (UP)	0	215.586	0.031	0.999	8.787	−81.847
Model			297.434	0.032_1	(1.0)	–	–

† n is the number of electrons redistributed at random. ‡ n is the number of electrons in fragment. § Minimum value of correlation coefficients between the total reconstructed density and the model density; the correlation coefficients were computed in sections along **c** in the cell. ¶ $\Delta q^{err}(\mathbf{x}) = q^{ME}(\mathbf{x}) - q^{model}(\mathbf{x})$.

total electron density in silicon (Takata & Sakata, 1996). In that work, a complete data set was obtained from the one of Saka & Kato (1986) by taking out the 844 and 880 reflections, but in doing so the resolution of the data set was also decreased from 0.479 to 0.581 Å; it is therefore difficult to disentangle the combined effect of resolution and completeness on the quality of the resulting map.

We have already shown here that valence-only calculations (*A* and *B*) can reconstruct the model density within an acceptable error: this is true in spite of the data-set incompleteness. To provide further evidence for the fact that artefacts observed in Takata & Sakata (1996) do not arise from data incompleteness but mainly from the inadequacy of the method to reconstruct total densities without a structural model for the core, we have repeated a calculation similar to the one described by de Vries, Briels, Feil, te Velde & Baerends (1996): *BUSTER* has been run against a set of 42 synthetic data that is complete up to 0.479 Å, except for the nine forbidden reflections. This calculation is labelled *G*. The electron-density profile along [111] is shown in Fig. 14. The false peak at the Si—Si midpoint is still present, although the value of the density is now correct within 3%. The value of the density at the nucleus is 227.94 e Å^{-3}, still off by as much as 23%. Greater data completeness does improve the quality of the map but does not eliminate artefacts.

To check the resolution dependence of the results, an all-electron calculation was also performed from a uniform prior, fitting the 125 allowed reflections (plus the forbidden 222) out of the 155 up to 0.317 Å resolution. The electron-density profile is the one labelled *H* in Fig. 14. The value of the electron density is close to that for calculation *G*, but a broad modulation is still present, creating a very shallow maximum at the bond midpoint. It is seen that even extension of the data set to very high resolution cannot give back the correct topology at this position.

6.2. *Beryllium*

A model density was computed with *VALRAY* for crystalline beryllium by a fit to 58 structure-factor amplitudes measured at room temperature by Larsen & Hansen (1984). The space group is $P6_3/mmc$, one Be atom in the asymmetric unit at site $2(c)$, $(\frac{1}{3}\frac{2}{3}\frac{1}{4})$. The multipolar model applies anharmonic corrections to the temperature factor, expansion of the atomic density up to $l = 4$, and single exponential deformation functions.

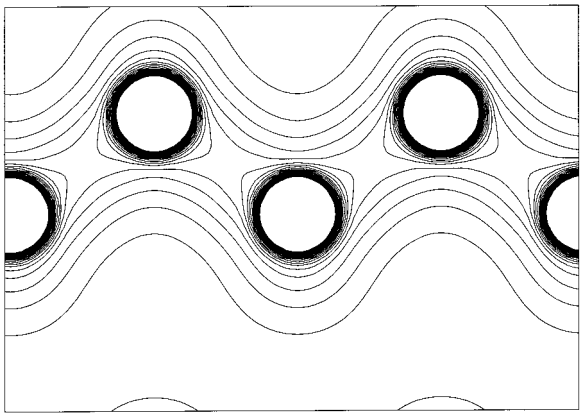

Fig. 5. Silicon. Dynamic model density $q^{model}(\mathbf{x})$ in section (110). Map 7.68 Å (along $[1\bar{1}0]$, horizontal) × 5.43 Å (along [001], vertical). Contours: from 0.0 to 2.50 e Å^{-3}, step 0.1 e Å^{-3}. $q(\mathbf{x})^{model}_{min} = 0.032$; $q(\mathbf{x})^{model}_{max} = 297.43$ e Å^{-3}.

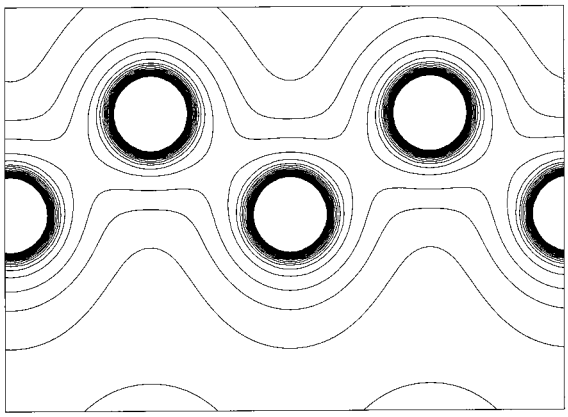

Fig. 6. Silicon. All-electron NUP of spherical atoms $m(\mathbf{x}) = q^{IAM}_{val}(\mathbf{x})$ in section (110). Map size and contouring level as in Fig. 5. $m_{min}(\mathbf{x}) = 0.062$; $m_{max}(\mathbf{x}) = 297.360$ e Å^{-3}.

Harmonic atomic displacement parameters and electronic population parameters for the *K*-shell and *L*-shell monopole functions and for the symmetry-allowed quadrupole, octopole and hexadecapole were varied. Coefficients up to fourth order in the cumulant expansion of the the temperature factor were kept fixed to values obtained from the Gram–Charlier coefficients in Iversen *et al.* (1995). Convergence was reached to statistical indexes: $R(F) = 0.0033$, $wR(F) = 0.0035$, $R(F^2) = 0.0069$, $wR(F^2) = 0.0069$; G.o.f. = 1.431.

At variance with the silicon study described above, 'idealized' core and monopole population parameters equal to 2 electrons were then used to compute the synthetic density, while other parameters retained the values from the above refinement. Positivity of the valence density obtained with this model was checked on a uniform grid in the asymmetric unit. The model dynamic density was initially generated on a $64 \times 64 \times 96$ grid; this number of divisions subsequently proved insufficient to sample the density at the nucleus, in that the nuclear position does not fall on any of the grid points: the interpolated value is too low by 1.5% with respect to a model density sampled on a $120 \times 120 \times 192$ grid.† Sections in plane (110) of the model dynamic density and of the all-electron prior-prejudice distribution obtained by core and valence monopoles are shown in Fig. 15.

58 structure factors were calculated up to the experimental resolution limit, 0.417 Å. Table 3 lists some of the significant quantities for all the *BUSTER* calculations performed against this data set, together with the values relative to the model density.

6.2.1. *Valence-only calculations*. Against this synthetic data set, two valence-only calculations were performed, using a fragment of *K*-shell electrons and redistributing the *L*-shell electrons with a nonuniform prior prejudice of *L*-shell monopoles (calculation *A*) and with a uniform prior prejudice (calculation *B*). All ME valence densities were generated on a $64 \times 64 \times 96$ grid.

Fig. 16 shows the error maps in the (110) section of the crystal for calculations *A* and *B*. The maps are devoid of features below 0.005 e Å^{-3}, except in the nuclear regions where the error remains below 0.03 e Å^{-3} in absolute value anyway. For the beryllium valence density, whose dynamic range is around 3, reconstruction is satisfactory even when a uniform prior-prejudice distribution is used.

6.2.2. *All-electron calculations*. The *total* structure factors were now used as target values in two all-electron calculations modulating a nonuniform prior prejudice of *K*- and *L*-shell monopoles (*C*) and a uniform prior prejudice (*D*). Calculation *D* corresponds to the one described by Iversen *et al.* (1995); the same work mentions a calculation equivalent to *C*; more recently, both types of calculation have been described by de Vries, Briels & Feil (1996). Reconstruction of the total density by modulation of the uniform prior-prejudice distribution required a finer grid in calculation *D* ($120 \times 120 \times 192$).

From the section of the electron density in Fig. 17(*b*), it is already apparent that *D* does not reconstruct the model density well. Density *D* underestimates the value of the density at the nucleus by about 3.8% and has wiggly contours in low-density regions. In particular, there is accumulation of charge at position 2(*d*) in the basal plane; this position is at the bipyramidal space between the two tetrahedral cavities above and below the basal plane, along the *c* axis. This point is the one marked with an asterisk in the section of the *D* density of Fig. 17(*b*). It is at this position that one of the NNM's has been found by Iversen *et al.* (1995).

Fig. 18 shows the error maps in the (110) section of the crystal for calculations *C* and *D*. Concentric shells of

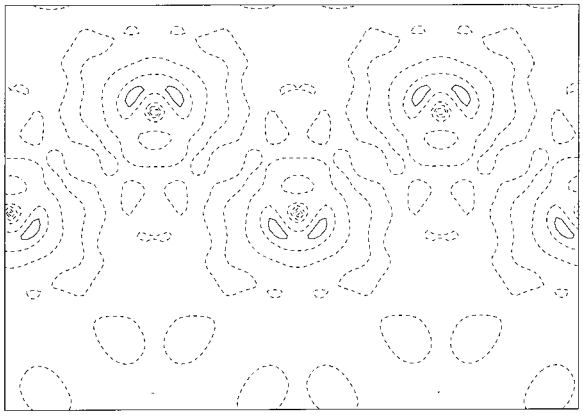

Fig. 7. Silicon. Calculation *A*: $\Delta q(\mathbf{x})^{\rm err}$ in section (110). Section 7.68 × 5.43 Å ([001]). Contours: −1.5 to 0.49 e Å^{-3}, step 0.01 e Å^{-3}. $\Delta q(\mathbf{x})^{\rm err}_{\rm min} = -0.049$; $\Delta q(\mathbf{x})^{\rm err}_{\rm max} = 0.014$ e Å^{-3}.

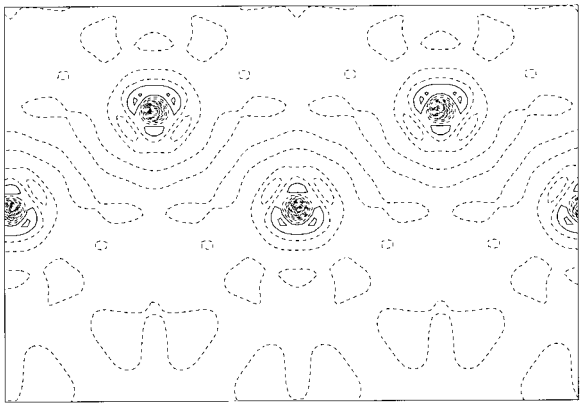

Fig. 8. Silicon. Calculation *B*: $\Delta q(\mathbf{x})^{\rm err}$ in section (110). Map size and contour levels as in Fig. 7. $\Delta q(\mathbf{x})^{\rm err}_{\rm min} = -0.112$; $\Delta q(\mathbf{x})^{\rm err}_{\rm max} = 0.022$ e Å^{-3}.

† This is a general problem in ME studies, where the sampling of the density at the nuclear position can in some cases only be performed by choosing the grid appropriately (see Carvalho *et al.*, 1996; Ishibashi *et al.*, 1994).

positive and negative residuals peak around the atoms. Notice that for calculation *D* the error in the nuclear region (-1.835 e Å^{-3}) is below the minimum contouring level and was not contoured.

The density around position 2(*d*) was more closely inspected by plotting total electron-density profiles through this point along the [1$\bar{1}$0] and [001] directions (Fig. 19). Abscissae in both graphs are fractional distances, *z* along the *c* axis and d/d_0 along the longer base diagonal of the hexagonal cell, respectively, for the [001] and [1$\bar{1}$0] directions. In the plot at the top of Fig. 19, the density profile along [001] clearly shows that along this direction site 2(*d*) is a maximum in all densities but, while reconstruction is accurate for calculations *A*–*C*, density *D* has an excess of about 1% at site 2(*d*) ($z = \frac{2}{4}$). The bottom plot shows that density *D* at site 2(*d*) ($d/d_0 = \frac{2}{3}$) is not only too high but also presents the wrong curvature in the basal plane: this point erroneously becomes a maximum along [1$\bar{1}$0] also. An artificial NNM is created at site 2(*d*) by the redistribution of core electrons in the random part with the uniform prior.

These results confirm those reported by de Vries, Briels & Feil (1996) but give further insight about the origin of the spurious details observed, which depends on the amount of missing structure rather than on the use of a uniform prior-prejudice distribution. In fact, for valence densities having such a small dynamic range as that of beryllium, the core–valence partitioning scheme first implemented in *BUSTER* allows for reconstruction of the density from noise-free data even with a uniform prior prejudice (calculation *B*).

6.2.3. *Further tests. NNM reconstruction*. A model density containing a NNM at position 2(*d*) was generated with *VALRAY* by placing an H atom at ($\frac{2}{3}\frac{1}{3}\frac{1}{4}$), with a monopole population of 0.005 electrons and an isotropic displacement parameter $U_{iso} = 0.03$ Å^2. Synthetic structure factors up to 0.417 Å resolution were used in a valence-only calculation similar to *A*, with a fragment of Be *K*-shell electrons and a nonuniform prior prejudice of Be *L*-shell electrons *without* the H atom. The total electron-density profile along [1$\bar{1}$0] at $z = \frac{1}{4}$ is shown in Fig. 20, together with the model density. *BUSTER* was clearly able to detect the presence of the NNM at site 2(*d*).

Use of a biased prior-prejudice distribution. In a sense, the dependence of the method to biased prior-prejudice distributions has already been tested when performing calculations *B* and *D*, with the uniform prior prejudice for the valence and total density, respectively. We have also tested the bias from a nonuniform prior obtained by a superposition of Be *L*-shell monopoles plus an H atom placed, as described above, at site 2(*d*). This biased valence prior prejudice has been used in a calculation (*F*) with the usual *K*-shell core fragment for Be and Be *L*-shell valence electrons in the random part (like calculation *A*).

Fig. 21 shows profiles along the [1$\bar{1}$0] direction at $z = \frac{1}{4}$ for the valence density of the model, the ME valence density of calculation *F* and the biased valence prior. The valence ME distribution from calculation *F* is virtually indistinguishable from that of the model and correctly shows no local maximum at site 2(*d*): the false detail present in the prior prejudice is wiped out on the basis of the information contained in the observations.

Fit to high-resolution data. A synthetic data set of 116 reflections complete up to 0.317 Å has been computed from the model density of beryllium and an all-electron run performed, modulating a uniform prior prejudice, as in calculation *D*. This calculation is labelled *G*. The grid used was $144 \times 144 \times 240$.

Fig. 22 shows the (110) section of the resulting ME distribution. The corresponding total electron-density profile is shown in Fig. 23 together with the model density profile. The artificial NNM at site 2(*d*) has disappeared but the density has distorted contours. This

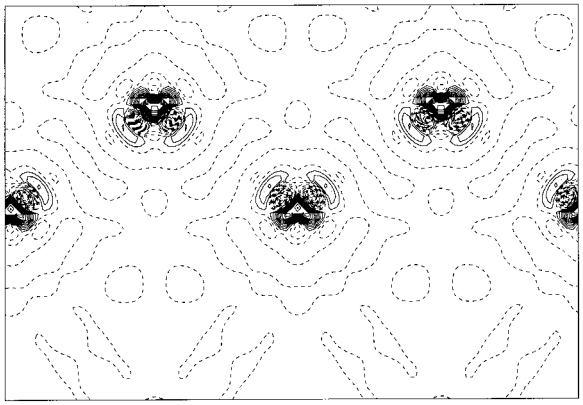

Fig. 9. Silicon. Calculation *C*: $\Delta q(\mathbf{x})^{\rm err}$ in section (110). Map size and contour levels as in Fig. 7. $\Delta q(\mathbf{x})^{\rm err}_{\rm min} = -0.169$; $\Delta q(\mathbf{x})^{\rm err}_{\rm max} = 0.142$ e Å^{-3}.

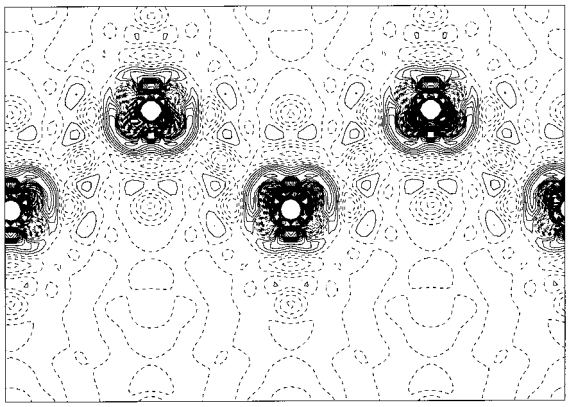

Fig. 10. Silicon. Calculation *D*: $\Delta q(\mathbf{x})^{\rm err}$ in section (110). Map size and contour levels as in Fig. 7. $\Delta q(\mathbf{x})^{\rm err}_{\rm min} = -0.903$; $\Delta q(\mathbf{x})^{\rm err}_{\rm max} = 6.735$ e Å^{-3}. Maximum and minimum values exceed the traced contour levels.

Table 3. *Summary of BUSTER runs on model synthetic data for crystalline beryllium*

Densities were sampled on a 64 × 64 × 96 grid, except where otherwise stated.

Density	$24 \times n$†	$12 \times n_{\rm frag}$‡	$q_{\rm max}$	$q_{\rm min}$	$CC_{\rm min}$§	$\Delta q^{\rm err}_{\rm max}$¶	$\Delta q^{\rm err}_{\rm min}$
A	2 (NUP)	2	49.729	0.180	0.999_8	0.003	−0.016
B	2 (UP)	2	49.721	0.180	0.999_7	0.004	−0.024
C	4 (NUP)	0	49.775	0.180	0.999_6	0.030	−0.010
D††	4 (UP)	0	48.674	0.179	0.997	0.277	−1.835
Model		2+2	49.733‡‡	0.180	(1.0)	–	–
Model‡		2+2	50.496	0.180	(1.0)	–	–

† n is the number of electrons redistributed at random. ‡ n is the number of electrons in fragment. § Minimum value of correlation coefficients between the total reconstructed density and the model density; the correlation coefficients were computed in sections along **c** in the cell. ¶ $\Delta q^{\rm err}(\mathbf{x}) = q^{\rm ME}(\mathbf{x}) - q^{\rm model}(\mathbf{x})$. †† Density on a 120 × 120 × 192 grid. ‡‡ Grid is not adequate to sample the density at the nuclear position.

is in keeping with the results shown for the all-electron run for silicon and confirms that, even in the presence of very high resolution data, all-electron runs with a uniform prior-prejudice distribution cannot reconstruct the atomic cores and low-density regions of the structure.

6.3. *Discussion*

6.3.1. *The 'frozen-core approximation'*. The use of core fragments represents an improvement over the redistribution of all of the electrons in the random part: the latter approach would carry over to biasing the final picture by a deep ignorance about the existence of atomic cores in the crystal. The validity of this 'frozen-core approximation' can be questioned but this is a general problem in charge-density studies, which also assume that the static picture of the core density be unaltered on passing from gas phase to the solid, so that electron-density distributions for the atomic core can be transferred by *ab initio* calculation for the isolated atoms.

Evidence of the contrary is sometimes found in the literature. For example, a 0.5% expansion of the atomic core and an enhanced thermal vibration of the same core density with respect to the valence density have been found for Si (Lu *et al.*, 1993). Core expansion in solid beryllium has also been advocated to explain the higher values of the atomic displacement parameters obtained from a fit to high-order X-ray data as compared with the values from a neutron refinement (Larsen & Hansen, 1984). Evidence for the need of core deformation functions was also obtained for beryllium by Stewart (1977). Recently, a 0.182 Å neutron diffraction study on MnF_2 has given indirect confirmation of a polarization of the inner shell of the F atoms owing to antiferromagnetic order in the crystal (Jauch *et al.*, 1996).

Usually, either the data do not contain information about the core structure or, even when they do, the parameterization of the core-electron distribution is not flexible enough to model it. In fact, as pointed out by Lu, Zunger & Deutsch (1993) in their study of crystalline diamond, silicon and germanium, the conventional choice for radial deformation functions $R_l(r)$ is such that $R_{l\neq 0}(r = 0) = 0$, so that, at the nuclear positions, the only contributions to the deformation density come from the tails of the radial functions of higher poles

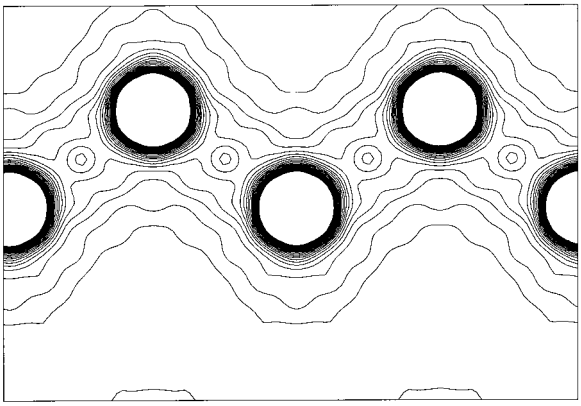

Fig. 11. Silicon. Calculation *F*: total density. Map size and contour levels as in Fig. 5. $q(\mathbf{x})^F_{\rm min} = 0.032$; $q(\mathbf{x})^F_{\rm max} = 215.576\,{\rm e\,\AA^{-3}}$.

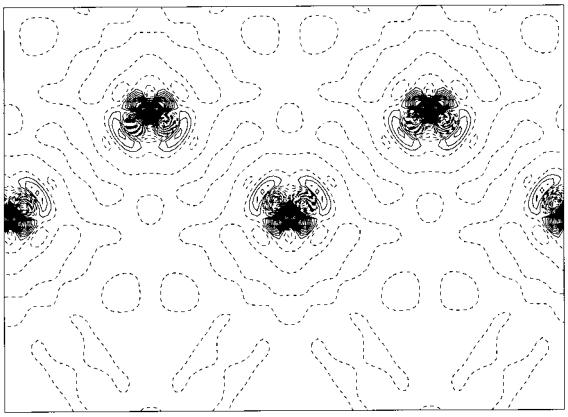

Fig. 12. Silicon. Calculation *E*: $\Delta q(\mathbf{x})^{\rm err}$. Map size and contour levels as in Fig. 7. $\Delta q(\mathbf{x})^{\rm err}_{\rm min} = -0.187$; $\Delta q(\mathbf{x})^{\rm err}_{\rm max} = 0.438\,{\rm e\,\AA^{-3}}$.

($l > 0$) centred at neighbouring nuclei. The flexibility of the model used to describe the core regions is therefore limited, attention being focused on the valence density.

Obviously, the picture for the ME valence-electron density depends at present on the description given for the fragment, in terms of the scale factor, core monopole populations and positional and atomic displacement parameters. Moreover, the present implementation can correct the model adopted for the atomic core only by the modulation introduced by the non-negative tails of the ME valence density in the same region.

6.3.2. *Various choices for the prior prejudice*. The problem remains of assessing to what extent the results are dependent on the particular nonuniform prior chosen. Hansen & Wilkins (1996) have recently tried to generalize the maximum-entropy approach by introducing the concept of 'distributions of prior-prejudice distributions'.

In the present approach, the choice of a prior distribution of electrons is not really different from other structural hypotheses, such as phases to be attached to the experimental structure-factor amplitudes or parameters in the model for the partial structure and could therefore be subjected to likelihood tests against the data.

A range of possible departures of the distributions of the valence electrons from $m(\mathbf{x})$ can be explored; the possible choices for $m(\mathbf{x})$ can be specified in a variety of ways, such as explicit phase assignments for the amplitudes of the worst agreeing structure factors or various modulations of $m(\mathbf{x})$ by parameterized multipole terms. The ME calculations, in the manner in which they have been used to improve on direct methods, will give log-likelihood gains for each of these hypotheses with respect to the null hypothesis: a statistical analysis of these will show whether the data point significantly towards any of them. Other types of hypotheses might consist of assuming certain values of multipole coefficients to describe the distribution of a subpopulation of valence electrons; only the remaining valence electrons would be dealt with by the maximum-entropy method, with a revised $m(\mathbf{x})$, to evaluate the log-likelihood gains; the multipole coefficients could then be refined by maximizing that gain. This would allow for the modelling of negative valence densities, which might be required given the core–valence partitioning scheme adopted; negative valence densities cannot be obtained by ME distribution, but could be obtained by maximum-likelihood refinement of multipolar parameters in the NUP.

This new approach to multipolar refinement, using maximum likelihood rather than least squares as a refinement criterion, has the advantage that it can deal not only with measurement errors on amplitudes but also with the uncertainty of phase values in the case of noncentrosymmetric structures. An illustration of the use of likelihood in valence-density reconstruction of a noncentrosymmetric structure was given by Roversi *et al.* (1998). It is clear though that, if insufficient information is contained in the data, there might be no means of discriminating between several possible choices for $m(\mathbf{x})$; it is nevertheless encouraging that tests with biased $m(\mathbf{x})$ show some 'robustness' with respect to the choice of $m(\mathbf{x})$, at least on noise-free data (see §6.2.3).

6.3.3. *The experimental error variances*. Within the computational scheme described here, the use of one Lagrange multiplier per structure-factor component can naturally prevent the uneven distributions of residuals observed in the case of a single χ^2 restraint. As pointed out by Carvalho *et al.* (1996), the handling of one

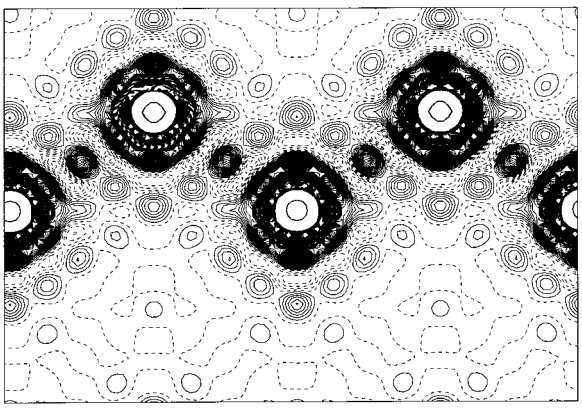

Fig. 13. Silicon. Calculation *F*: $\Delta q(\mathbf{x})^{\rm err}$. Map size and contour levels as in Fig. 7. $\Delta q(\mathbf{x})^{\rm err}_{\rm min} = -81.856$; $\Delta q(\mathbf{x})^{\rm err}_{\rm max} = 8.508\,{\rm e\,\AA^{-3}}$. Maximum and minimum values exceed the traced contour levels.

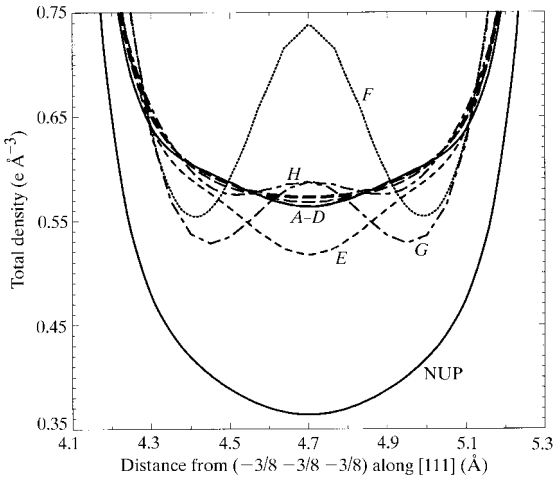

Fig. 14. Silicon. Total electron-density profile along [111] in between two bonded Si atoms. The reconstructed electron-density profiles for calculations *A–D* (long-dashed lines) all closely follow the one for the model electron density (solid line). The profiles for calculations *F*, *G* and *H* (dotted and dot-dashed lines) show artifical charge accumulation at the midpoint of the bond. The lower curve is the density profile for the nonuniform prior prejudice of *K*-, *L*- and *M*-shell monopoles used in calculation *E*.

constraint per datum is a very demanding numerical task; in our experience, the duality algorithm implemented into *BUSTER* (Bricogne, 1991*a*) has proven very robust in handling up to 2600 individual constraints.

All calculations described here have been carried out on noise-free synthetic data, for which the exact targeting of structure-factor amplitudes is of no concern. Dealing properly with experimental error variances needs assessment of the effective number of scatterers to bring the variances computed from the random scatterer model on the scale of the observed ones. Each observation is then fitted within the experimental error. A preliminary report about the first results obtained with *BUSTER* on noisy data is being published (Roversi *et al.*, 1998).

7. Concluding remarks

The observations presented here are in keeping with the general notion that the maximum-entropy method is best understood as a method for testing hypotheses against the experimental data, in the presence of some prior knowledge. In a crystallographic context, the Bayesian viewpoint on crystal structure determination prescribes the use of the maximum-entropy method to perform iterative testing of structural hypotheses and allow model updating (Bricogne, 1988*a*, 1997).

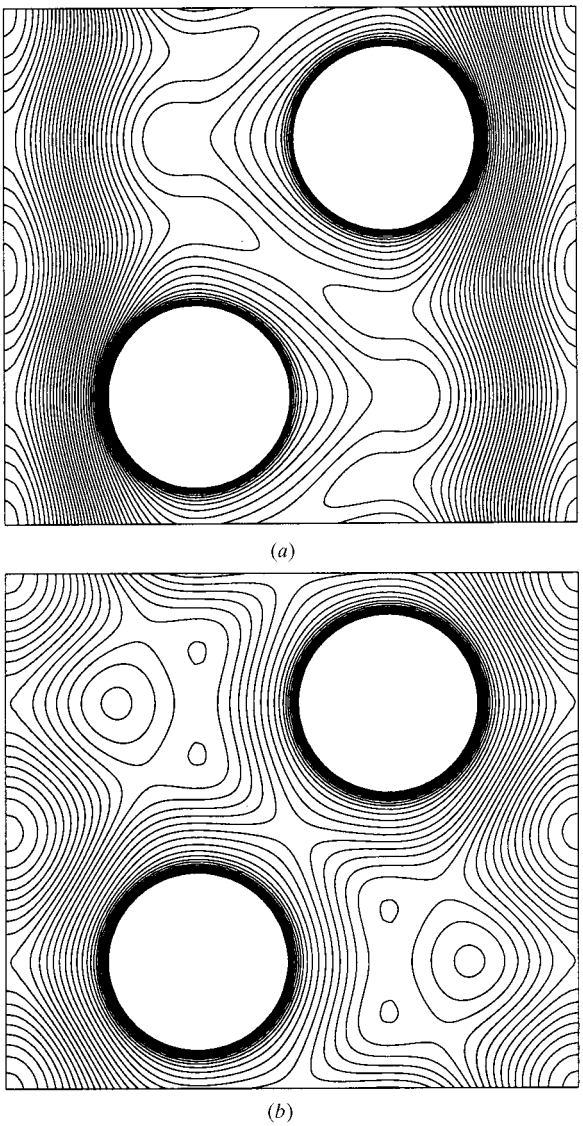

Fig. 15. Beryllium. Model dynamic density in section (110). Map size: 3.97 Å ([1$\bar{1}$0], horizontal) × 3.58 Å ([001], vertical). Map centre at ($\frac{1}{2}\frac{1}{2}\frac{1}{2}$). Contour levels: from 0.180 to 0.312 e Å^{-3}, step 0.003 e Å^{-3}. (*a*) Total dynamic density. (*b*) Procrystal dynamic density.

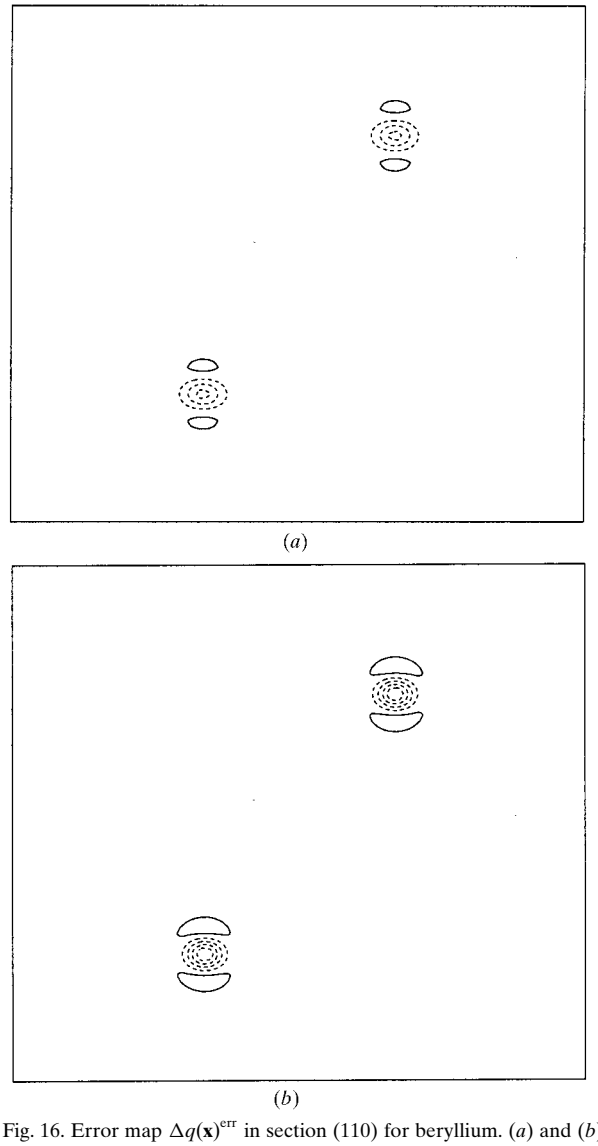

Fig. 16. Error map $\Delta q(\mathbf{x})^{\rm err}$ in section (110) for beryllium. (*a*) and (*b*): calculations *A* and *B*, respectively. Map size as in Fig. 15. Contours from −0.0306 to 0.0294 e Å^{-3}, step 0.0053 e Å^{-3}.

From this viewpoint, it is possible to rationalize the results of the different types of charge-density ME calculations discussed so far. In each case, the calculation provides an answer whose quality is commensurate with the degree of adequacy or inadequacy of the null hypothesis made; these null hypotheses can be ranked in increasing order of information content:

(i) Many of the MaxEnt calculations described in the literature ignore any knowledge of the atomicity of structures other than that conveyed by the choice made for the target structure-factor phases (see §2): a uniform prior is used, and all electrons are redistributed under the maximum-entropy condition. The resulting distribution already contains a clear picture of atoms, with atomic cores and bonding density regions; but the topology of these MaxEnt densities will often be wrong because the missing structure is not adequately modelled by random independent constituents (Roversi, Irwin & Bricogne, 1996).

(ii) Within the computational scheme described in the course of this work, the available information about the atomic substructure (core + valence) can be taken into account explicitly. In the simplest possible calculation, a fragment of atomic cores is used and a ME distribution for valence electrons is computed by modulation of a uniform prior prejudice. As we have shown in the noise-

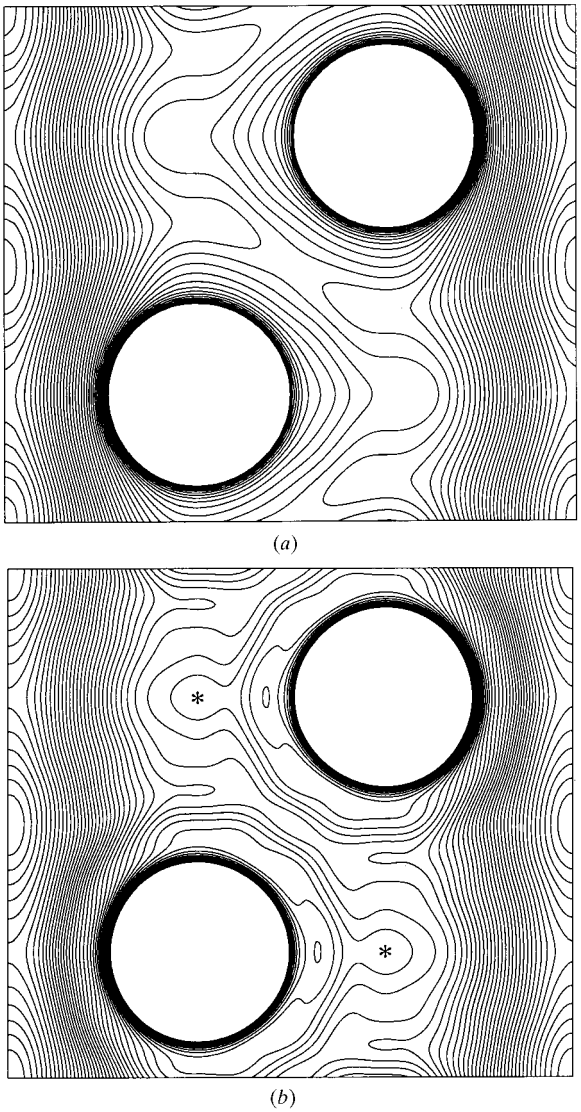

Fig. 17. Beryllium. ME total dynamic densities. (*a*) Calculation *A*, the density is reconstructed as in formula (26) by a core fragment and a valence ME map with $m(\mathbf{x}) = q_{\rm val}^{\rm IAM}(\mathbf{x})$. (*b*) Calculation *D*, all-electron ME map obtained with a uniform prior prejudice. Map size and orientation and contouring levels as in Fig. 15.

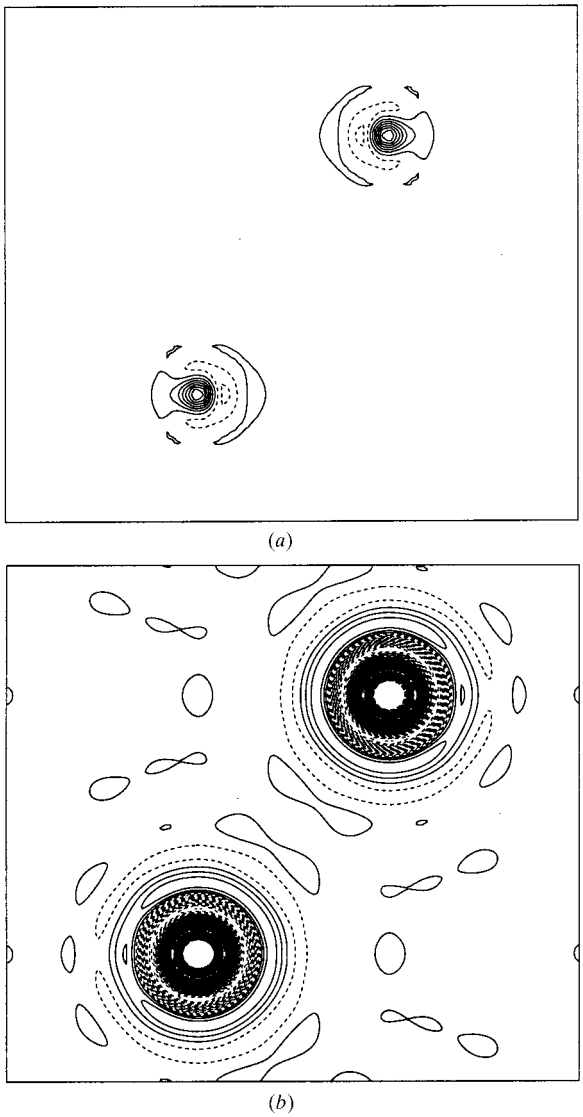

Fig. 18. Error map $\Delta q(\mathbf{x})^{\rm err}$ in section (110) for beryllium. Calculations *C* and *D*. Map size and orientation as in Fig. 15. The contouring level scheme is the same as the one in Fig. 16; in the error map for calculation *D*, too large a negative error in the nuclear region gets truncated.

free calculations on α-glycine described in §4.1.1, the method will yield a better representation of bonding and nonbonding valence-charge concentration regions but bias will still be present because of Fourier truncation ripples and aliasing errors.

(iii) Full atomicity can be incorporated into the available prior information using a nonuniform prior prejudice of spherical-valence shells, together with the atomic core fragment. The test presented in §4.1.1 shows that it is possible to correctly reconstruct the aspherical features in the density, in the absence of experimental noise. At this stage, no stereochemical knowledge has yet been used, other than that implicitly conveyed by the geometry of the nuclear framework. The presence of the experimental noise would soften the constraints imposed by the observations, so that multiple-order bonds and very sharp nonbonded charge concentration features will still be deflated (Roversi *et al.*, 1998).

(iv) The next update of the null hypothesis would incorporate a zero-order description of bonding in terms of a prior prejudice of 'standard' chemical groups. The transferability of standard multipolar parameters from a peptide databank have already been tested and proven effective in improving refinement of small proteins (Pichon-Pesme *et al.*, 1995): an additional test of the extent to which standard deformation terms are transferable from one system to another would be provided by building aspherical priors from deformation-density databases. The ME map then will tell us about the subtle differences induced in formally equivalent chemical bonds by conjugation, stacking and other intra- and intermolecular interactions. To achieve this degree of accuracy, the refinement of structural parameters present in the model adopted for the fragment should proceed together with the ME redistribution of the valence electrons.

We have described in this paper the first implementation of this Bayesian approach to charge-density studies, making joint use of structural models for the atomic core substructure and ME distributions of scatterers for the valence part. Used in this way, the maximum-entropy method is 'safe' and can usefully complement the traditional modelling based on finite multipolar expansions. This supports our initial proposal that accurate charge-density studies should be viewed as the late stages of the structure determination process.

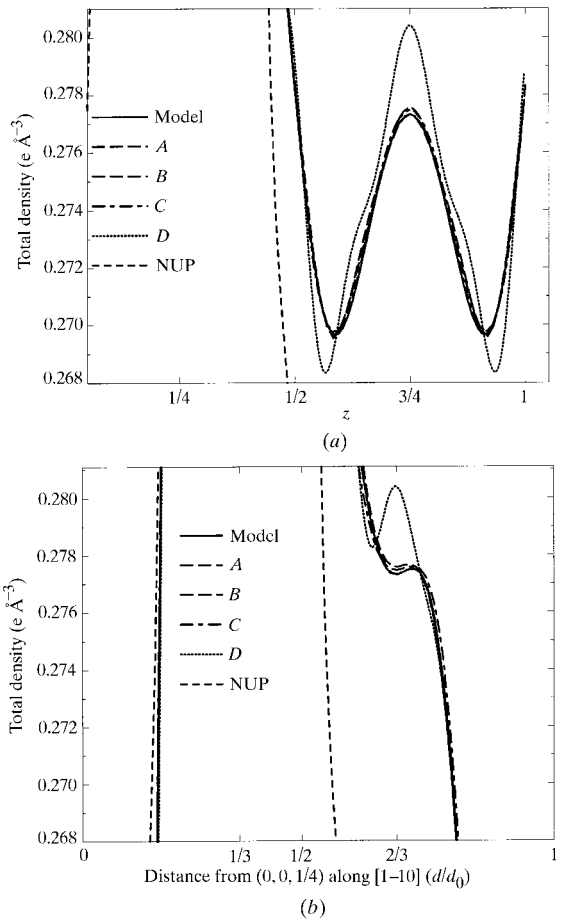

Fig. 19. Beryllium. Total dynamic electron-density profiles along [001], going through special position 2(*d*). Abscissae in both graphs are fractional distances. (*a*) [001] direction, **z** along the *c* axis, $x = \frac{1}{3}, y = \frac{2}{3}$. (*b*) [1$\bar{1}$0] direction and d/d_0 along the longer base diagonal of the hexagonal cell, $z = \frac{1}{4}$. Solid line: model density. Long-dashed line: calculations *A* and *B*. Dot-dashed line: calculation *C*. Density for calculation *D* (dotted line) shows excess density and the wrong topology at position 2(*d*).

APPENDIX *A*
Dynamic electron density by aliasing

BUSTER reconstructs the total electron density as shown in formula (26): the prior-prejudice distribution and the fragment density need to be sampled on the same grid upon which the ME calculation is performed.

Both the prior-prejudice distribution and the fragment density are model dynamic densities. If Gaussian-type basis functions are used to expand the static atomic densities, the sampling of model dynamic densities on crystallographic grids can be performed using an analytical expression for the thermally smeared density in real space (Stewart & Flensburg, 1998). No tractable analytical form exists for the thermally smeared density when the multipolar expansion for the static atomic density is a linear combination of Slater-type functions, as is the case in the majority of charge-density studies to date.

For this reason, dynamic densities are usually sampled numerically on a grid by Fourier transformation of their structure factors. The resulting density is accurate provided two simple conditions are met: all structure factors greater than the numerical threshold have to be included in the sum, in order to avoid series-termination

Table 4. *Summary of structures for which periodized structure factors were generated and dynamic density computed*

Structure	Space group	Formula	Atoms per cell	T (K)	$1/d^*_{\mathbf{h}}$ (Å)
α-Glycine	$P2_1/c$	$C_2H_5NO_2$	40	23	0.436
L-Alanine	$P2_12_12_1$	$C_3H_7NO_2$	52	23	0.463
Citrinin	$P2_12_12_1$	$C_{13}H_{14}O_5$	128	20	0.438
Pyrope	$Ia\bar{3}d$	$Mg_{1/4}Al_{1/6}Si_{1/4}O$	160	30	0.438
Triglycine	$P\bar{1}$	$2(C_6H_{11}N_3O_4)$	96	120	0.464
HMT	$I\bar{4}3m$	$C_{1/4}H_{1/2}N_{1/6}$	44	298	0.452
Be	$P6_3/mmc$	$Be_{1/12}$	2	298	0.417
Diopside	$C2/c$	$Ca_{1/2}Mg_{1/2}SiO_3$	40	298	0.434
Si	$Fd\bar{3}m$	$Si_{1/24}$	8	298	0.480

ripples; the sampling grid must be fine enough to accommodate the resolution of the same nonzero structure factors and prevent aliasing errors (Brigham, 1974) in the sampled density (Shannon, 1949; Bricogne, 1993*b*).

As mentioned above, the ME grid is chosen on the basis of the prior-prejudice bandwidth and on the amplitudes of the Lagrange multipliers entering the exponential model of the density. This grid might not be fine enough to adequately sample the fragment density by simple numerical Fourier transform of its nonzero structure factors: the latter might extend to a resolution well beyond the one of the data set fitted. It is usually not possible to sample fragment densities on the ME grid by simple FFT of its Fourier coefficients.

This problem could be overcome by choosing the ME grid on the basis of the Shannon grid needed to sample the fragment density. This would demand additional computational effort, especially when dealing with low-temperature data sets for crystals containing some heavy atom, whose core electrons scatter to very high order. Alternatively, one could sample the fragment density by FFT of its nonzero Fourier coefficients on its Shannon grid, and then interpolate it on the coarser grid used for the ME calculation.

A third solution is the one implemented in the course of this work, and it is described in this Appendix. The method is very general and allows for error-free sampling of model densities on any grid, no matter how coarse: it is based on the particular instance of the convolution theorem known as the duality between periodization and sampling (Bricogne, 1993*b*).

The most common example of this duality belongs to the basics of crystallography, whereby the periodic electron density of the crystal is expressed as the convolution of the electron density in the unit cell with a lattice distribution of Dirac δ functions having the translational symmetry of the crystal lattice itself: sampling of the Fourier transform of the electron density in the cell then occurs at the nodes of the dual lattice, giving nonzero structure factors only for integer Miller indices.

If the rôles of the real and reciprocal space are reversed in the latter example, it is seen that numerical Fourier transform of a set of structure factors, rendered

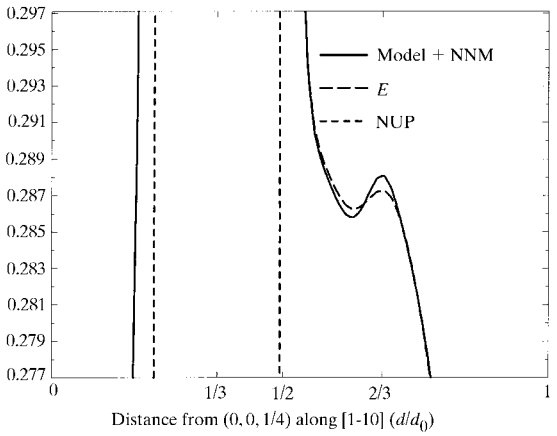

Fig. 20. Reconstruction of a NNM arbitrarily placed at site 2(*d*) in the beryllium cell. Solid line: total model dynamic electron-density profile along $[1\bar{1}0]$ in the basal plane at $z = \frac{1}{4}$. Long-dashed line: calculation *E*. Dashed line: spherical-atom dynamic density. The prior prejudice was built from spherical beryllium valence shells with no knowledge of the density at the special position.

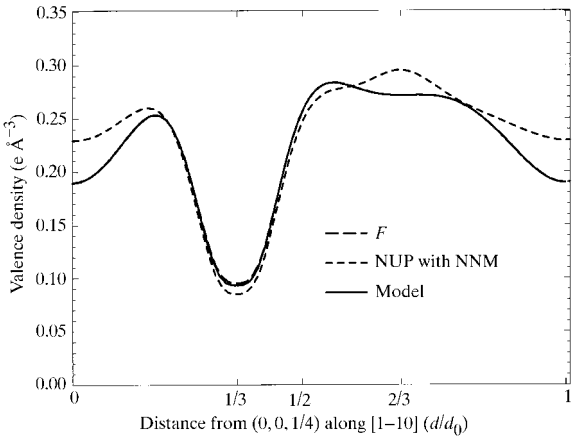

Fig. 21. Beryllium. Calculation *F*: the prior-prejudice distribution includes a NNM at site 2(*d*) which was not in the model. Dynamic valence-electron-density profiles along $[1\bar{1}0]$ in the basal plane at $z = \frac{1}{4}$. Solid line: model valence density. Dot-dashed line: calculation *F*. Dashed line: nonuniform prior of spherical valence shells + NNM at site 2(*d*). The false detail in the prior-prejudice distribution is correctly wiped out in the ME reconstruction.

periodic by a lattice reciprocal to an arbitrary real-space lattice-grid, will cause the density to be sampled on the same grid in real space. To sample any model density on a given grid, it is therefore sufficient to periodize its Fourier coefficients along a grid reciprocal to the given sampling grid, and to Fourier transform the set of periodized structure factors.

This computational scheme had already been implemented into *BUSTER* to effectively sample macromolecular envelopes blurred in reciprocal space by means of an overall temperature factor (Bricogne, 1994). We describe here the implementation of the algorithm within the computer program *VALRAY* (Stewart & Spackman, 1983), which has enabled the sampling of prior-prejudice distributions and fragment densities on the grids chosen for the *BUSTER* ME calculations.

Let Λ^* be a reciprocal lattice consisting of the vectors $\boldsymbol{\xi}$:

$$\boldsymbol{\xi} = h\mathrm{NX}\mathbf{a}^* + k\mathrm{NY}\mathbf{b}^* + l\mathrm{NZ}\mathbf{c}^*,$$

where (NX, NY, NZ) are three positive integers and $\mathbf{a}^*$, $\mathbf{b}^*$ and $\mathbf{c}^*$ are the basis vectors of the reciprocal lattice of the crystal. Let $\mathbf{R}^*$ be a lattice distribution built from the Λ^* lattice:

$$\mathbf{R}^* = \sum_{\xi \in \Lambda^*} \delta(\boldsymbol{\xi}).$$

$\mathbf{R}^*$ is used to periodize the structure-factor distribution $\mathbf{F}$:

$$\mathbf{F}^{\mathrm{alias}} = \mathbf{R}^* * \mathbf{F}. \tag{28}$$

The convolution in (28) renders $\mathbf{F}^{\mathrm{alias}}$ periodic under translations by vectors in Λ^*:

$$\mathbf{F}^{\mathrm{alias}}(\mathbf{h}) = \tau_{\xi}\mathbf{F}^{\mathrm{alias}}(\mathbf{h}) = \mathbf{F}^{\mathrm{alias}}(\mathbf{h} - \boldsymbol{\xi}).$$

If we now call $\mathbf{R}$ the lattice distribution dual to $\mathbf{R}^*$, $\mathbf{R} = \mathcal{F}[\mathbf{R}^*](\mathbf{x})$, we can write

$$\mathbf{R} = \sum_{\mathbf{x} \in \Lambda} \delta(\mathbf{x}),$$

where the vectors $\mathbf{x}$ belong to the Λ lattice:

$$\mathbf{x} = (m/\mathrm{NX})\mathbf{a} + (n/\mathrm{NY})\mathbf{b} + (p/\mathrm{NZ})\mathbf{c} \quad m, n, p \in Z.$$

The Fourier transform of the periodic distribution $\mathbf{F}^{\mathrm{alias}}$ can be written, making use of the convolution theorem, as

$$\begin{aligned}\mathcal{F}[\mathbf{F}^{\mathrm{alias}}](\mathbf{x}) &= \mathcal{F}[\mathbf{R}^* * \mathbf{F}](\mathbf{x}) \\ &= (\mathrm{NX})(\mathrm{NY})(\mathrm{NZ})|\det \mathbf{A}^*|^{-1}\mathbf{R} \cdot \mathcal{F}[\mathbf{F}]\mathbf{x} \\ &= (\mathrm{NX})(\mathrm{NY})(\mathrm{NZ})|\det \mathbf{A}^*|^{-1} \sum_{\mathbf{x} \in \Lambda} \rho^0(\mathbf{x})\delta(\mathbf{x}) \\ &= \sum_{\mathbf{x} \in \Lambda} \rho^0(\mathbf{x})\delta(\mathbf{x}) \end{aligned} \tag{29}$$

($\mathbf{A}^*$ is the matrix whose columns are the basis vectors of the Λ^* lattice). It is apparent that the Fourier transformation samples the cell electron density at the nodes of the Λ lattice.

The convolution with the lattice of delta functions in (28) requires in principle an infinite number of translates. In practice, it is sufficient to take into account only those structure factors that are above some numerical precision threshold; in this work, structure-factor amplitudes lower than 10^{-7} have been neglected. In fact, the calculation begins by assessing a resolution limit past which all structure factors can safely be assumed to be negligible, based on the known fall-off of atomic scattering factors with resolution. The resolution limit can be expressed in terms of maximum Miller indices for structure factors to enter the sum. Then,

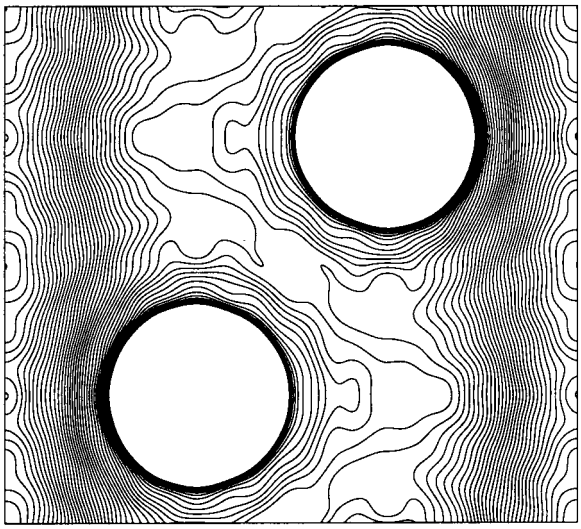

Fig. 22. Beryllium. Calculation *G*. Dynamic total density. Fit to 116 model structure factors up to 0.317 Å. Map size and orientation and contour levels as in Fig. 15.

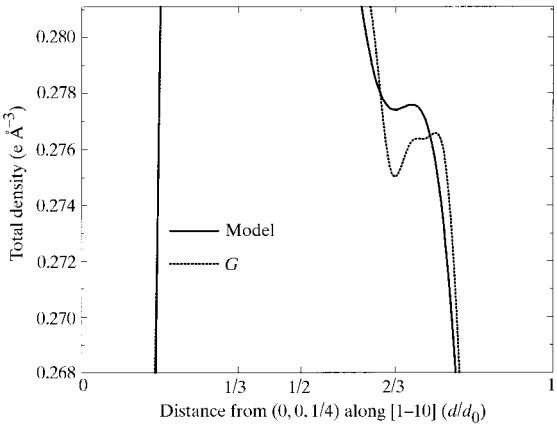

Fig. 23. Beryllium. Total dynamic electron-density profile along $[1\bar{1}0]$ in the basal plane at $z = \frac{1}{4}$. Solid line: dynamic model density. Dotted line: calculation *G*.

Table 5. *Resolution limits in the aliasing sum (30) for the structures in Table 4*

Structure	NX, NY, NZ†	$d_{\mathbf{h}}^{\min} TF$ (Å)‡	$d_{\mathbf{h}}^{\min}$ (Å)§	$H_{\max}, K_{\max}, L_{\max}$	No. of copies¶
α-Glycine	64, 144, 72	0.062	0.083	65, 142, 71	8
L-Alanine	64, 128, 64	0.063	0.085	69, 144, 68	24
Citrinin	144, 76, 144	0.066	0.090	147, 80, 135	16
Pyrope	120, 120, 120	0.039	0.047	245, 245, 245	48
Triglycine	120, 128, 48	0.082	0.099	117, 148, 48	16
HMT	76, 76, 76	0.179	0.279	25, 25, 25	4
Be	64, 64, 96	0.082	0.103	18, 18, 29	4
Diopside	96, 96, 64	0.061	0.069	141, 129, 76	28
Si	144, 144, 144	0.083	0.113	52, 52, 52	4

† Number of points along reciprocal axes for the periodizing lattice Λ^*. The grid is the one needed in *BUSTER* for a valence-only ME calculation. ‡ Resolution threshold past which all atomic temperature factors fall below 10^{-7}. § Resolution threshold past which all atomic *dynamic* scattering factors fall below 10^{-7}. ¶ Number of periodizing lattice vectors entering the sum in (30).

$$\mathbf{F}^{\text{alias}}(\mathbf{h}) = \mathbf{R}^* * \mathbf{F}(h,k,l) = \sum_{m=-H_{\max}}^{H_{\max}} \sum_{n=-K_{\max}}^{K_{\max}} \sum_{p=-L_{\max}}^{L_{\max}} \times \mathbf{F}(h - m\text{NX}, k - n\text{NY}, l - p\text{NZ}). \quad (30)$$

Real and imaginary parts of aliased structure factors are only needed in a reciprocal-space prism having dimensions (NX, NY, NZ) because of the periodic nature of the $\mathbf{F}^{\text{alias}}$: moreover, the Hermitian symmetry of the structure factors allows a reduction of the number of $\mathbf{F}^{\text{alias}}$ by a factor of two. The Miller indices in (30) are therefore being varied in the ranges $0 \le h \le \text{NX}/2$, $0 \le k \le \text{NY} - 1$, $0 \le l \le \text{NZ} - 1$. The density is then synthesized by FFT from the $\mathbf{F}^{\text{alias}}$ values.

The number of periodizing vectors needed in the sum in (30) depends on the overlap between the translates of the nonzero structure factors and the original copy around (000). Four copies suffice when the grid chosen is fine enough to satisfy the Shannon criterion for the density to be sampled. In this case, there is no overlap in reciprocal space between the original copy and any of the translates; the aliasing procedure is tantamount to sheer Fourier transform of the nonzero set of structure factors. Whenever the grid is too coarse to allow proper sampling by Fourier transform, the aliasing procedure will run over more than four translating vectors. Table 4 lists the structures used to test the implementation and Table 5 reports typical values obtained.

This work was partially supported by an International Research Scholarship from the Howard Hughes Medical Institute (to GB) and by a collaborative research grant from Pfizer Central Research (to GB). Digital Equipment Corporation generously loaned the Alpha workstations used for the calculations. Riccardo Destro and Finn Krebs Larsen kindly made their diffraction data available to us. Mark Spackman and Bob Stewart assisted us with the *VALRAY* programming. Thanks are also due to Carlo Gatti and Eric de La Fortelle for useful discussions.

References

Alkire, R., Yelon, W. & Schneider, J. (1982). *Phys. Rev. B*, **26**, 3097–3104.
Bader, R. F. W. (1990). *Atoms in Molecules. A Quantum Theory.* The International Series of Monographs in Chemistry. Oxford University Press.
Beek, C. van, Overeem, J., Ruble, J. & Craven, B. (1996). *Can. J. Chem.* **74**, 943–950.
Bricogne, G. (1984). *Acta Cryst.* A**40**, 410–445.
Bricogne, G. (1988*a*). *Acta Cryst.* A**44**, 517–545.
Bricogne, G. (1988*b*). *Crystallographic Computing*, Vol. 4, edited by N. Isaacs & M. Taylor, pp. 60–79. IUCr/Oxford University Press.
Bricogne, G. (1991*a*). *Crystallographic Computing*, Vol. 5, edited by D. Moras, A. D. Podjarny & J. C. Thierry, pp. 257–297. Oxford: Clarendon Press.
Bricogne, G. (1991*b*). *Acta Cryst.* A**47**, 803–829.
Bricogne, G. (1991*c*). *Maximum Entropy in Action*, edited by B. Buck & V. A. Macaulay, pp. 187–216. Oxford University Press.
Bricogne, G. (1992). *Molecular Replacement*, Proceedings of the CCP4 Study Weekend, SERC Daresbury Laboratory, Warrington, England, pp. 62–75.
Bricogne, G. (1993*a*). *Acta Cryst.* D**49**, 37–60.
Bricogne, G. (1993*b*). *International Tables for Crystallography*, Vol. B, *Reciprocal Space*, edited by U. Shmueli, pp. 23–106. Dordrecht: Kluwer Academic Publishers.
Bricogne, G. (1994). Unpublished results.
Bricogne, G. (1997). *Methods Enzymol.* **276**, 361–423.
Bricogne, G. & Gilmore, C. J. (1990). *Acta Cryst.* A**46**, 284–297.
Bricogne, G. & Irwin, J. J. (1996). *Macromolecular Refinement*, Proceedings of the CCP4 Study Weekend, SERC Daresbury Laboratory, Warrington, England, pp. 85–92.
Brigham, O. (1974). *The Fast Fourier Transform.* New York: Prentice Hall.
Brown, A. S., Spackman, M. A. & Hill, R. J. (1993). *Acta Cryst.* A**49**, 513–527.
Carter, C. W. Jr, Crumley, K. V., Coleman, D. E., Hage, F. & Bricogne, G. (1990). *Acta Cryst.* A**46**, 57–68.
Carvalho, C., Hashizume, H., Stevenson, A. & Robinson, I. (1996). *Physica (Utrecht)*, B**221**, 469–486.
Chen, R., Trucano, P. & Stewart, R. F. (1977). *Acta Cryst.* A**33**, 823–828.
Clementi, E. (1965). *IBM J. Res. Dev.* **9**, Part 2.

Destro, R. (1998). Personal communication.
Destro, R. & Merati, F. (1995). *Acta Cryst.* B**51**, 559–570.
Dong, W., Baird, T., Fryer, J., Gilmore, C., MacNicol, D., Bricogne, G., Smith, D. J., O'Keefe, M. & Hövmoller, S. (1992). *Nature (London)*, **355**, 605–609.
Doublié, S., Bricogne, G., Gilmore, C. J. & Carter, C. W. Jr (1995). *Structure*, **3**, 17–31.
Doublié, S., Xiang, S., Gilmore, C. J., Bricogne, G. & Carter, C. W. Jr (1994). *Acta Cryst.* A**50**, 164–182.
El Haouzi, A., Hansen, N., Le Hénaff, C. & Protas, J. (1996). *Acta Cryst.* A**52**, 291–301.
Flensburg, C., Larsen, S. & Stewart, R. F. (1995). *J. Phys. Chem.* **99**, 10130–10141.
Gilmore, C. J. (1996). *Acta Cryst.* A**52**, 561–589.
Gilmore, C. J., Bricogne, G. & Bannister, C. (1990). *Acta Cryst.* A**46**, 297–308.
Gilmore, C. J., Henderson, K. & Bricogne, G. (1991). *Acta Cryst.* A**47**, 830–841.
Hansen, S. & Wilkins, S. W. (1996). *Acta Cryst.* A**52**, 547–550.
Hendrickson, W. & Lattman, E. (1970). *Acta Cryst.* B**26**, 136–143.
Howard, S., Hursthouse, M., Lehmann, C. & Poyner, E. (1995). *Acta Cryst.* B**51**, 328–337.
Ishibashi, H., Shimimoto, K. & Nakahigashi, K. (1994). *J. Phys. Chem. Solids*, **55**(9), 809–814.
Iversen, B. B., Jensen, J. L. & Danielsen, J. (1997). *Acta Cryst.* A**53**, 376–387.
Iversen, B. B., Larsen, F. K., Figgis, B. N. & Reynolds, P. A. (1997). *J. Chem. Soc. Dalton Trans.* pp. 2227–2240.
Iversen, B. B., Larsen, F. K., Souhassou, M. & Takata, M. (1995). *Acta Cryst.* B**51**, 580–591.
Jauch, W. (1994). *Acta Cryst.* A**50**, 650–652.
Jauch, W. & Palmer, A. (1993). *Acta Cryst.* A**49**, 590–591.
Jauch, W., Schultz, A. J. & Stewart, R. F. (1996). *Acta Cryst.* A**52**, C344.
Jaynes, E. (1957*a*). *Phys. Rev.* **106**, 620–630.
Jaynes, E. (1957*b*). *Phys. Rev.* **108**, 171–190.
Jaynes, E. (1968). *IEEE Trans. Syst. Sci. Cybernetics*, **SSC-4**, 227–241.
Jaynes, E. (1983). *Papers on Probability, Statistics and Statistical Physics*, edited by R. D. Rosenkrantz. Dordrecht: Reidel.
Larsen, F. K. & Hansen, N. K. (1984). *Acta Cryst.* B**40**, 169–179.
Lecomte, C. (1995). Personal communication.
Lu, Z. & Zunger, A. (1992). *Acta Cryst.* A**48**, 545–554.
Lu, Z., Zunger, A. & Deutsch, M. (1993). *Phys. Rev. B*, **47**, 9385–9410.
Nowack, E., Schwarzenbach, D. & Hahn, T. (1991). *Acta Cryst.* B**47**, 650–659.
Papoular, R. J. & Gillon, B. (1990). *Europhys. Lett.* **13**(5), 429–434.
Papoular, R. J., Vekhter, Y. & Coppens, P. (1996). *Acta Cryst.* A**52**, 397–407.
Pichon-Pesme, V., Lecomte, C. & Lachekar, H. (1995). *J. Phys. Chem.* **99**, 6242–6250.
Restori, R. & Schwarzenbach, D. (1995). *Acta Cryst.* B**51**, 261–263.
Roversi, P., Barzaghi, M., Merati, F. & Destro, R. (1996). *Can. J. Chem.* **74**, 1145–1161.
Roversi, P., Irwin, J. J. & Bricogne, G. (1996). *Acta Cryst.* A**52**, C343.
Roversi, P., Irwin, J. & Bricogne, G. (1998). In *Charge, Spin and Momentum Densities and Chemical Reactivity*, edited by P. G. Mezey & B. Robertson. Dordrecht: Kluwer Academic Publishers. In the press.
Saka, T. & Kato, N. (1986). *Acta Cryst.* A**42**, 469–478.
Sakata, M. & Sato, M. (1990). *Acta Cryst.* A**46**, 263–270.
Sakata, M., Uno, T., Takata, M. & Howard, C. (1993). *J. Appl. Cryst.* **26**, 159–165.
Schiltz, M., Shepard, W., Fourme, R., Prangé, T., de La Fortelle, E. & Bricogne, G. (1997). *Acta Cryst.* D**53**, 78–92.
Shannon, C. E. (1949). *Proc. Inst. Radio Eng.* **37**, 10–21.
Smith, G. (1997). PhD thesis, Durham University, England.
Souhassou, M., Espinosa, E., Lecomte, C. & Blessing, R. H. (1995). *Acta Cryst.* B**5**1, 661–668.
Souhassou, M., Lecomte, C., Ghermani, N.-E., Rohmer, M.-M., Wiest, R., Bénard, M. & Blessing, R. H. (1992). *J. Am. Chem. Soc.* **114**, 2371–2382.
Spackman, M. (1986). *Acta Cryst.* A**42**, 271–281.
Spackman, M. & Brown, A. S. (1994). *Ann. Rep. R. Soc. Chem.* pp. 175–212.
Stewart, R. F. (1977). *Acta Cryst.* A**33**, 33–38.
Stewart, R. F. (1980). *Electron and Magnetization Densities in Molecules and Crystals*, edited by P. Becker, pp. 427–431. New York: Plenum Press.
Stewart, R. F. & Flensburg, C. (1998). Personal communication.
Stewart, R. F. & Spackman, M. (1983). *VALRAY Users Manual*, 1st ed. Carnegie-Mellon University, Pittsburgh, PA 15213, USA.
Takata, M. & Sakata, M. (1996). *Acta Cryst.* A**52**, 287–290.
Takata, M., Sakata, M., Kumazawa, S., Larsen, F. & Iversen, B. (1994). *Acta Cryst.* A**50**, 330–337.
Terpstra, M., Craven, B. M. & Stewart, R. (1993). *Acta Cryst.* A**49**, 685–692.
Voigt-Martin, I., Yan, D., Yakimansky, A., Schollmeyer, D., Gilmore, C. J. & Bricogne, G. (1995). *Acta Cryst.* A**51**, 849–868.
Vries, R. de, Briels, W. & Feil, D. (1994). *Acta Cryst.* A**50**, 383–391.
Vries, R. de, Briels, W. & Feil, D. (1996). *Phys. Rev. Lett* **77**, 1719–1722.
Vries, R. de, Briels, W., Feil, D., te Velde, G. & Baerends, E. (1996). *Can. J. Chem.* **74**, 1054–1058.
Xiang, S., Carter, C. W. Jr, Bricogne, G. & Gilmore, C. J. (1993). *Acta Cryst.* D**49**, 193–212.
Yamamoto, K., Takahashi, Y., Ohshima, K., Okamura, F. & Yukino, K. (1996). *Acta Cryst.* A**52**, 606–613.
Zheludev, A., Papoular, R. J., Ressouche, E. & Schweizer, J. (1995). *Acta Cryst.* A**51**, 450–455.
Zou, P. F. & Bader, R. F. W. (1994). *Acta Cryst.* A**50**, 714–725.